MASTER IN QUANTUM SCIENCE AND TECHNOLOGY

Spinor Bose–Einstein Condensate Magnetometry for Searches in Fundamental Physics

Wenjing Zhou

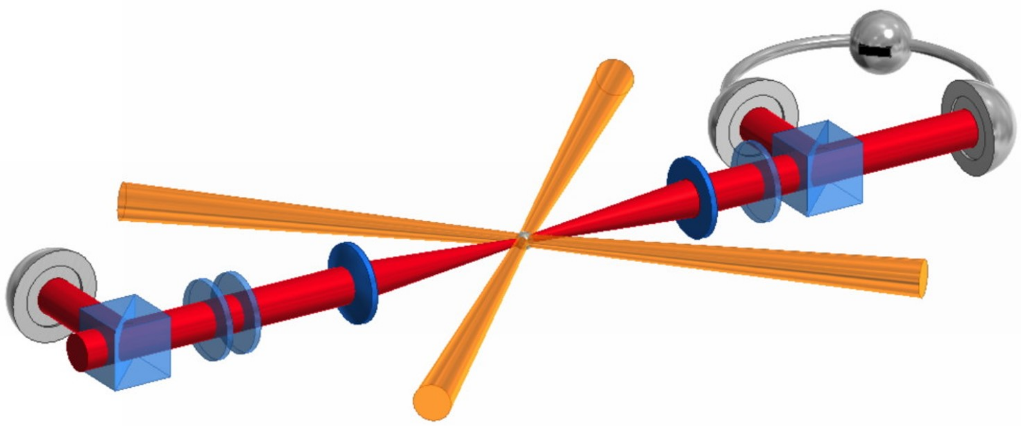

Supervisors
Prof. Dr. Morgan Mitchell
Prof. Dr. Diego Blas

Academic year
2024/25

Spinor Bose–Einstein Condensate Magnetometry for Searches in Fundamental Physics

Wenjing Zhou

Supervised by: Prof. Dr. Morgan Mitchell, Prof. Dr. Diego Blas

ICFO, Mediterranean Technology Park, Avinguda Carl Friedrich Gauss, 3, 08860 Castelldefels, Barcelona

7 July 2025

This thesis investigates the use of a Spinor Bose-Einstein Condensate as a micrometer-scale quantum sensor for probing new fundamental physics. The sensor's sensitivity is limited by a complex interplay of noise sources. We develop a theoretical framework to identify, model, and quantify these limitations, using the truncated Wigner approximation to capture interaction-induced shearing of the quantum noise and project sensitivity beyond the standard quantum limit. This model is supported by experimental efforts, including finite-element method simulations of an apertured magnetic shield and the development of a shot-noise-limited Faraday polarimeter. Applying the full framework, we show that an SBEC comagnetometer can set improved laboratory constraints on axion-like particle–proton couplings. In contrast, we find that the sensor's small interaction volume limits its competitiveness for detecting high-frequency gravitational waves via spin-gravity coupling.

Keywords: Quantum Sensing, Quantum Metrology, Spinor Bose-Einstein Condensate, Magnetometry, Comagnetometry, Dark Matter, Axion-like Particles, Gravitational Waves, Exotic Spin-dependent Interactions, Pseudomagnetic Fields, Truncated Wigner Approximation, Standard Quantum Limit, Magnetic Shielding, Faraday Rotation.

Wenjing Zhou: Wenjing.Zhou@icfo.eu

Acknowledgements

First of all, I want to thank my two main supervisors, Diego and Morgan.

Diego has been guiding me since my Bachelor's thesis, and I feel very lucky to continue working with him. He is a true *jefazo* — always very busy, but always generous with his time and ideas. His way of thinking is bold and imaginative, and I really appreciate how he approaches physics almost like art — drawing concepts on paper with an elegance that takes time to fully understand, but always feels rewarding. After every meeting, I would spend hours unpacking the equations and trying to follow the trail, and I loved it. Working with him has definitely shaped the way I see theoretical physics.

That project also led me to meet Morgan — soon to be my PhD supervisor (yes, it's happening!). I'm truly grateful for his guidance and support. He's an exceptional group leader: not only knowledgeable and sharp, but also incredibly generous with his time and attention. No matter how busy he is, he always takes our questions seriously, and his answers always push us to think more deeply. I also really appreciate the atmosphere he's built in the group — open, curious, and collaborative. I took two of his courses this year, and even the exams were enjoyable (which says a lot!). They were carefully designed, and actually helped me learn. I can honestly say he has shaped the way I think about physics, and working with him has played a big role in how much I've grown this year — in intuition, in curiosity, and in confidence.

I also want to thank Ola, our amazing postdoc! Officially, she's not listed as my supervisor, but she has been guiding me from the start. She's been incredibly kind, always there to teach me things in the lab, and made every workday feel easier and more fun. I honestly admire her a lot—she's skilled, smart, and just a great person to be around. I've learned so much from her, and I feel lucky to share the office with her.

To my teammates in the BEC group—Zoi, Bertran, and Greg! Thank you for being such kind and supportive colleagues. You've all been so generous with your time and knowledge, especially in the lab, and I've learned a lot from each of you. Greg, I always enjoy our physics discussions; they've helped me understand many concepts more clearly.

Thanks also to everyone else in the AQO group. There are too many names to list here, but I've really appreciated how welcoming and friendly everyone has been.

This year has been intense, but in a good way. I really enjoyed working on this project. The hardest part, to be honest, has been writing this thesis (which I'm still doing. . .). But it's been worth it!

And on my birthday, I designed an SBEC-themed cake for our team. I'll leave a photo below to remember it :)

Figure 1: An SBEC-themed Cake

Contents

1 Introduction

The search for physics beyond the Standard Model (BSM) calls for new types of sensors capable of detecting extremely weak signals. In this work, we use a Spinor Bose-Einstein Condensate (SBEC), a quantum sensor whose micrometer-scale size makes it especially well-suited to probing new interactions at short length scales [1]. We unify our search for new physics under the framework of detecting a pseudomagnetic field: an exotic field that induces spin precession in a manner analogous to a real magnetic field, but whose coupling strength is not proportional to the standard gyromagnetic ratio [2]. We apply this framework to two distinct physical phenomena that manifest as pseudomagnetic fields: the fields generated by a new spin-dependent force mediated by the exchange of Axion-Like Particles (ALPs), and the oscillating fields induced by the interaction of a passing high-frequency gravitational wave (GW) with the atoms in the sensor.

A BEC is a macroscopic quantum object formed by cooling a dilute gas of atoms to nanokelvin temperatures, where thousands of atoms occupy the same quantum ground state and are described by a single wavefunction [3]. By confining the atoms in an all-optical trap, the spin degree of freedom is liberated. The resulting SBEC allows the collective spin of the entire ensemble to be used as a highly sensitive sensing element.

The simplest sensing modality is a magnetometer, which measures the Larmor precession angle $\theta^{(f)} = \gamma^{(f)} \int B(t)dt$ of the collective spin in a single hyperfine manifold. However, the high sensitivity to external magnetic fields is also its primary weakness, as signals from new physics are typically overwhelmed by ambient magnetic noise. To overcome this, we operate the system as a comagnetometer. This technique uses a coherent superposition of the $F = 1$ and $F = 2$ hyperfine manifolds, which possess nearly opposite gyromagnetic ratios due to their internal spin structure. The summed precession angle, $\theta^{(12)} = \theta^{(1)} + \theta^{(2)}$, is sensitive only to the small nuclear magnetic contribution, providing a common-mode rejection of magnetic field noise of approximately 48 dB [1] while retaining full sensitivity to non-magnetic, spin-dependent interactions.

The performance of these quantum sensors is determined by the interplay of several noise sources. The readout noise, arising from the measurement apparatus, is dominated by the fundamental photon shot noise (PSN) of the probe light used for non-destructive Faraday probing [4]. The atoms themselves are subject to atomic quantum noise. The fundamental floor for this is the spin projection noise (SPN), which arises from the quantum uncertainty of measuring a finite ensemble of N atoms and defines the standard quantum limit (SQL). However, in an SBEC, many-body collisional interactions introduce an additional noise source. The competition between the ferromagnetic spin-exchange interaction and the quadratic Zeeman (QZ) shift drives coherent spin-mixing dynamics, which distorts, or "shears," the initial quantum noise distribution [5]. This shearing noise often presents a more stringent practical limit than the SQL.

This thesis is structured as follows. Sec. 2 develops the theoretical framework for the SBEC as a quantum sensor, from the Single-Mode Approximation Hamiltonian to a quantum noise model incorporating spin-mixing dynamics and particle loss to estimate sensitivity beyond the SQL. Sec. 3 presents two experimental subprojects developed in this work: FEM simulations of a magnetic shield with openings, and characterization of a shot-noise-limited Faraday polarimeter for non-destructive spin readout. Sec. 4 applies the full framework to search for new physics: (i) projecting constraints on ALP couplings via monopole-dipole interactions sourced by Earth and a tungsten mass; (ii) compute the projected strain sensitivity to high-frequency GWs based on the non-relativistic dynamics of a spinor in curved spacetime. Sec. 5 concludes with a summary and outlook.

2 Theoretical Framework

In this chapter, we build the theoretical foundation for the spinor BEC sensor. We start by deriving the effective Hamiltonian that governs its spin dynamics in the presence of external magnetic fields. We then introduce the comagnetometer scheme for noise rejection. Next, we define the fundamental sensitivity bound set by atomic projection noise. Finally, we go beyond this idealized picture using the truncated Wigner approximation (TWA) to simulate the full many-body dynamics and estimate the sensor's realistic performance.

2.1 Spinor BEC Magnetometry

We consider a magnetometer based on a spinor Bose-Einstein condensate (SBEC) of ^{87}Rb atoms in the $F = 1$ hyperfine manifold. To develop intuition about our system's quantum sensing capabilities, we first construct the theoretical model that captures its essential physics. The model is built upon a series of simplifications applied to the general description of a many-body quantum gas, which reduce the Hamiltonian to one governing the fundamental spin dynamics.

A complete description of an interacting N-particle quantum system is challenging. However, since ^{87}Rb is a weakly interacting gas, its dynamics and quantum statistics are well described by the mean-field approximation [3]. In this picture, quantum fluctuations and correlations are neglected at leading order [1]. The bosonic field operator $\hat{\Psi}(\mathbf{r})$ is approximated by its expectation value, a classical spinor order parameter $\Psi(\mathbf{r})$. The evolution of this order parameter is governed by the Gross-Pitaevskii equation (GPE), which is derived from a Hamiltonian split into spin-independent (H_{SI}) and spin-dependent (H_{SD}) parts [7]:

$$\begin{aligned} H_{SI} &= \int d^3\mathbf{r} \left(\Psi_\alpha^\dagger \left[-\frac{\hbar^2\nabla^2}{2M_{87}} + U(\mathbf{r}) \right] \Psi_\alpha + \frac{c_0}{2} \Psi_\alpha^\dagger \Psi_\beta^\dagger \Psi_\beta \Psi_\alpha \right), \\ H_{SD} &= \frac{c_2}{2} \int d^3\mathbf{r}\, \Psi_\alpha^\dagger F_{\alpha\beta}^\eta \Psi_\beta\, \Psi_\gamma^\dagger F_{\gamma\delta}^\eta \Psi_\delta + p \Psi_\alpha^\dagger F_{\alpha\beta}^z \Psi_\beta + q \Psi_\alpha^\dagger \left(F^z F^z\right)_{\alpha\beta} \Psi_\beta. \end{aligned} \tag{1}$$

Here, repeated spin indices are summed over, with $\alpha, \beta, \gamma, \delta$ running over the spin projections $m_F = -1, 0, +1$. The matrices $F^\eta (\eta = x, y, z)$ are the standard spin-1 angular momentum operators acting on the spinor components. The spin-independent part includes the kinetic energy, the trapping potential $U(\mathbf{r})$, and the contact interactions, set by c_0. Spin-dependent interactions scale with c_2, while p and q account for linear and quadratic Zeeman shifts from external fields.

While the GPE provides a complete mean-field description, it remains a set of coupled 3D partial differential equations. A further crucial simplification is the single-mode approximation (SMA) [8]. For a tightly confined condensate where spin-dependent interactions are weak, the kinetic energy cost of creating spatial variations in the spin texture is prohibitively high. This justifies the assumption that all atoms, regardless of their spin state, share the same spatial wavefunction $\phi(\mathbf{r})$. The order parameter can then be factorized as

$$\Psi(\mathbf{r}, t) = \phi(\mathbf{r})\chi(t). \tag{2}$$

Here, the complex spinor $\chi(t)$ contains the complete, spatially uniform spin dynamics of the N-atom ensemble. This approximation integrates out the spatial degrees of freedom, allowing us to focus on the internal spin dynamics of the collective state.

---

[1] In the mean-field approximation, the many-body quantum state is assumed to be a product of identical single-particle states, the field operator is approximated by its expectation value: $\hat{\Psi}(\mathbf{r}) \approx \langle \hat{\Psi}(\mathbf{r}) \rangle = \Psi(\mathbf{r})$. This neglects quantum fluctuations, $\delta\hat{\Psi} = \hat{\Psi} - \Psi$, and correlations, such as $\langle \hat{\Psi}^\dagger(\mathbf{r})\hat{\Psi}(\mathbf{r}') \rangle \approx \Psi^*(\mathbf{r})\Psi(\mathbf{r}')$, retaining only leading-order (classical field) contributions [6].

Substituting the SMA ansatz into the full Hamiltonian and integrating over space yields

$$H_{\mathrm{SMA}} = \mu + g\,\chi^{\dagger} F^{\eta}_{\alpha\beta}\chi_{\beta}\,\chi^{\dagger}_{\gamma} F^{\eta}_{\gamma\delta}\chi_{\delta} + p\,\chi^{\dagger}_{\alpha} F^{z}_{\alpha\beta}\chi_{\beta} + q\,\chi^{\dagger}_{\alpha}\left(F^{z}F^{z}\right)_{\alpha\beta}\chi_{\beta}. \tag{3}$$

The spin-independent terms contribute only a constant energy offset (the chemical potential, μ), which does not affect the spin dynamics and can be dropped. For ^{87}Rb atoms in the $F = 1$ state, the relevant s-wave scattering lengths a_0 and a_2 result in a negative interaction coefficient ($c_2 < 0$), making the interaction ferromagnetic[2].

The linear Zeeman (LZ) term, scaled by $p \equiv \hbar\omega_L$, drives the Larmor precession of the collective spin around the magnetic field. Since this rotation does not affect the relative spinor dynamics or populations, it can be eliminated by transforming to a rotating frame. After making these simplifications, we arrive at the SMA Hamiltonian that governs the non-trivial spin dynamics

$$H_{SMA} = g\chi^{\dagger}F\chi \cdot \chi^{\dagger}F\chi + q\chi^{\dagger}F_z^2\chi. \tag{4}$$

In this rotating frame, the internal spin evolution is governed by the competition between two nonlinear effects. The first is the quadratic Zeeman (QZ) shift, which arises from the second-order coupling of the magnetic field to the hyperfine structure and introduces an energy penalty proportional to m_F^2. This term energetically favors population in the $m_F = 0$ state over the $|m_F| = 1$ states. The second is the ferromagnetic spin-dependent interaction, which energetically favors states where the atomic spins are maximally aligned, thereby maximizing the collective spin length. This dynamic tension drives coherent spin-mixing dynamics, a collisional process where a pair of atoms in the $|1,0\rangle$ state can convert into a pair of atoms in the $|1,+1\rangle$ and $|1,-1\rangle$ states, and vice versa. This process continuously reshapes the quantum state, and is responsible for the orientation-to-alignment conversion [9] that we will explore in detail in Section 2.4.

The operational principle of the magnetometer is to perform a Ramsey-like measurement of the Larmor phase accumulated due to the LZ interaction. The collective spin of the prepared atomic ensemble precesses under the influence of the magnetic field, accumulating an angle $\theta^{(f)}$ over a free-evolution time $\mathcal{T}$:

$$\theta^{(f)}(\mathcal{T}) = \int_0^{\mathcal{T}} \gamma^{(f)} B(t)\,dt \tag{5}$$

The precision of this measurement, δB, is determined by how well the phase $\theta^{(f)}$ can be resolved over the optimal evolution time, set by the system's coherence time, t_{coh} . The single-shot precision is given by [6]:

$$\delta B = \frac{\delta\theta^{(f)}}{|\gamma^{(f)}|\,t_{coh}} \tag{6}$$

To compare performance between experiments, this single-shot precision is converted to a amplitude spectral density (ASD), $S_B^{1/2}$ (in $\mathrm{T}/\sqrt{\mathrm{Hz}}$) by scaling with the square root of the experimental cycle time, t_{cyc} , which accounts for the dead time between measurements. The high intrinsic sensitivity of this method, arising from the large electron gyromagnetic ratio ($\gamma^{(1)} \approx -\gamma_0$) and the long coherence times achievable in an SBEC, has been experimentally demonstrated on this apparatus, achieving a single-shot precision of 72(8) fT for a 3.5 s measurement [5].

---

[2] The validity of the SMA depends on the nature of spin-dependent interactions. For ferromagnetic interactions ($c_2 < 0$), as in ^{87}Rb, the SMA is valid in the mean-field ground state. In contrast, for antiferromagnetic interactions ($c_2 > 0$), the SMA can become invalid. In these systems, the interaction energy can favor the formation of spin textures, where different spin components develop distinct spatial profiles to lower the overall energy [8].

2.2 Spinor BEC Comagnetometry

The exceptional sensitivity of the spinor BEC magnetometer, as described in the previous section, is a double-edged sword. While it is highly responsive to the exotic fields that are the target of our search, it is equally sensitive to conventional magnetic field fluctuations present in any laboratory environment. These ambient field drifts are typically many orders of magnitude larger than the signals of interest and can easily overwhelm and mask the signature of new physics. To overcome this fundamental challenge, we operate the sensor not as a simple magnetometer, but as a comagnetometer. This technique uses two distinct but co-located sensors that respond similarly to the common-mode magnetic field noise, allowing it to be cancelled through a differential measurement.

In our system, we realize a comagnetometer by simultaneously preparing the atoms in a coherent superposition of the $F = 1$ and $F = 2$ ground-state hyperfine manifolds. These two manifolds act as our paired sensors. The key physical principle enabling noise cancellation is that they possess nearly opposite gyromagnetic ratios. This opposition arises from the different alignments of the electron spin ($\mathbf{S}$) and nuclear spin ($\mathbf{I}$). In the $F = 1$ state, the electron and nuclear spins are anti-aligned, whereas in the $F = 2$ state they are aligned. This results in gyromagnetic ratios [1] of $\gamma^{(1)} = -\gamma_0 - \gamma_s$ and $\gamma^{(2)} = +\gamma_0 - \gamma_s$, where $\gamma_0 \approx 2\pi \times 700\text{kHz/G}$ is the large contribution from the electron spin, and $\gamma_s \approx 2\pi \times 1.39\text{kHz/G}$ is the much smaller contribution from the nuclear spin.

Beyond the simple precession due to external fields, the rich internal dynamics of the comagnetometer are governed by spin-dependent collisional interactions. Within the SMA, the system's evolution is described by a Hamiltonian that includes the energies of and interactions between both manifolds:

$$H_{SMA} = E^{(1)} + E^{(2)} + \overline{E^{(12)}} \tag{7}$$

The full expressions for these energy terms, which account for all relevant Zeeman shifts and spin-exchange interactions, are detailed in Appendix A.

Instead of measuring a single precession angle, the comagnetometer readout is the sum of the angles accumulated by each manifold, $\theta^{(12)} = \theta^{(1)} + \theta^{(2)}$. The phase evolution of this summed angle due to an external magnetic field B is then:

$$\theta_B^{(12)} = \int \left(\gamma^{(1)} + \gamma^{(2)}\right) B(t)dt = \int \left(-2\gamma_s\right) B(t)dt \tag{8}$$

Crucially, the large electron contribution γ_0 cancels out, and the system's sensitivity to magnetic fields is now governed by the much smaller nuclear gyromagnetic ratio γ_s. This suppresses the instrument's response to common-mode magnetic noise by a factor of approximately $|\gamma_0/\left(2\gamma_s\right)| \approx 251$, or about 48 dB in power [1]. While this makes the system a poor magnetometer in the traditional sense, it becomes an exceptionally sensitive detector for non-magnetic effects that couple differently to the two manifolds, such as the pseudomagnetic fields of interest. The performance of such a sensor is benchmarked by its equivalent magnetic sensitivity, $S_B^{(12)}$. This figure of merit quantifies the magnetic field a standard magnetometer (with gyromagnetic ratio γ_0) would need to detect to achieve the same signal-to-noise ratio for an exotic interaction, and is given by:

$$S_B^{(12)} = \frac{\sqrt{t_{cyc}}}{\gamma_0 t_{coh}} \sqrt{\operatorname{Var}\left(\theta^{(12)}\right)} \tag{9}$$

where t_{coh} is the effective coherence time over which the spin phase evolves, and t_{cyc} is the total experimental cycle time, which includes the time required for state preparation and readout. Here, $\operatorname{Var}\left(\theta^{(12)}\right) = \operatorname{Var}\left(\theta_1\right) + \operatorname{Var}\left(\theta_2\right) + 2\operatorname{Cov}\left(\theta_1, \theta_2\right)$. A realistic estimation of this noise term using the TWA model will be a central topic of Sec. 2.4.

2.3 The Standard Quantum Limit (SQL)

The ultimate performance of any quantum sensor is constrained by a combination of noise sources. The most important noises for our experiments can be broadly categorized as: measurement noise, especially photon shot noise (see Sec. 3.3); systematic errors, including magnetic field fluctuations; and fundamental atomic quantum noise. This section focuses on the atomic spin projection noise, which defines the standard quantum limit (SQL).

The SQL represents a fundamental benchmark for sensitivity achievable using classical or non-entangled input states, such as the coherent spin states used in this work. While it is often considered a key performance goal, the SQL is not an absolute limit and can be surpassed using quantum resources like spin-squeezed states. It arises directly from the principles of quantum mechanics-specifically, the inherent uncertainty in measuring the spin projection of a finite ensemble of N atoms. Even in a perfectly prepared coherent spin state, quantum fluctuations introduce a minimum uncertainty in the outcome of a measurement.

A. SQL for the Magnetometer

We first derive the SQL-limited magnetic field sensitivity for a magnetometer operating with a single atomic ensemble. As shown in Appendix B, the fundamental quantum limit for measuring the precession phase of an ensemble of N atoms with total angular momentum F is the spin projection noise (SPN), given by $\delta\theta = 1/\sqrt{2NF}$. Inserting this into the formula for the single-shot precision (Eq. 6) gives:

$$\delta B = \frac{1}{|\gamma^{(f)}|\sqrt{2NF}} \cdot \frac{1}{t_{\text{coh}}} \tag{10}$$

To compare sensor performance, this single-shot precision is converted to an ASD, $S_B^{1/2}$, which has units of $\mathrm{T}/\sqrt{\mathrm{Hz}}$. The ASD is given by:

$$S_B^{1/2} = \delta B \cdot \sqrt{t_{cyc}} = \frac{\sqrt{t_{cyc}}}{|\gamma^{(f)}|\sqrt{2NF}t_{\text{coh}}} \tag{11}$$

We observe that in the best-case scenario, where $t_{\text{cyc}} = t_{\text{coh}}$, we recover Eq. (1) from [10]. Although $F = 1$ in our magnetometer, we retain F in the expressions to maintain generality.

B. SQL for the Comagnetometer

In the comagnetometer configuration, two ensembles in the $F = 1$ and $F = 2$ states are measured using spin-selective Faraday probing [1]. To derive the SQL, we assume ideal conditions: no particle loss, no backaction from interactions, and, crucially, that the quantum noises of the two atomic ensembles are completely uncorrelated. Under this assumption, the SQL-limited equivalent magnetic sensitivity, $S_{B,\text{ comag}}^{1/2}$ is given by:

$$S_{B,\text{ comag}}^{1/2} = \frac{\sqrt{t_{\text{cyc}}}}{\gamma_0 t_{\text{coh}}} \cdot \sigma_{\text{SQL}} \tag{12}$$

As derived in Appendix B, the total phase uncertainty from both ensembles at the SQL is $\sigma_{\text{SQL}} = \sqrt{\frac{3}{2N}}$. Substituting this into Eq. (12), we obtain the final SQL sensitivity for the comagnetometer:

$$S_{B,\text{ comag}}^{1/2} = \frac{\sqrt{t_{\text{cyc}}}}{\gamma_0 t_{\text{coh}}} \cdot \sqrt{\frac{3}{2N}} \tag{13}$$

2.4 Beyond the SQL: Truncated Wigner Approximation (TWA)

The SQL, as derived in Sec. 2.3, provides an essential benchmark for the best-case performance of our sensor. However, it is an idealized model that treats the atoms as a non-interacting ensemble. In a realistic SBEC, this picture is incomplete. The atoms are not isolated but form a complex, many-body quantum system where particle interactions, coherent spin-mixing dynamics, and inevitable particle losses all play crucial roles. These effects can significantly alter the system's coherence time and noise properties, causing the sensor's actual performance to deviate from the SQL. To build a predictive model that captures this rich, many-body physics, we must go beyond the SQL and employ a more sophisticated theoretical tool: the Truncated Wigner Approximation.

To account for decoherence from processes like atom loss, we model the system as an open quantum system whose evolution is described by a master equation ρ [7]:

$$\frac{d}{dt}\rho = \frac{1}{i\hbar}\left[H_{SMA}, \rho\right] + \mathcal{L}[\rho] \tag{14}$$

The first term describes the coherent evolution governed by the SMA Hamiltonian (Eq. 4), which captures the essential spin dynamics. The second term, the Liouvillian superoperator $\mathcal{L}[\rho]$, models the incoherent effects of system-environment coupling.

The central idea of the TWA is to map the quantum evolution of the many-body system onto a set of classical-like equations that can be solved numerically. For the comagnetometer, the quantum state is described by two coupled spinor field operators, for the $F = 1$ and $F = 2$ manifolds. In the TWA, these are replaced by two classical, complex-valued spinor vectors: $\mathbf{c}^{(1)} = (c_{+1}, c_0, c_{-1})^T$ and $\mathbf{c}^{(2)} = (c_{+2}, \ldots, c_{-2})^T$.

The evolution of this two-component system is governed by a set of coupled stochastic differential equations (SDEs) . The initial quantum noise is encoded by sampling initial conditions for $\mathbf{c}^{(1)}$ and $\mathbf{c}^{(2)}$ from the Wigner distribution of the prepared state . The SDEs for the system can be expressed conceptually as:

$$\begin{aligned} d\mathrm{c}^{(1)} &= \left(\mathrm{Drift}^{(1)}\right) dt + \left(\mathrm{Diffusion}^{(1)}\right) \cdot d\mathbf{Z} \\ d\mathrm{c}^{(2)} &= \left(\mathrm{Drift}^{(2)}\right) dt + \left(\mathrm{Diffusion}^{(2)}\right) \cdot d\mathbf{Z} \end{aligned} \tag{15}$$

Here, the deterministic Drift terms account for the coherent evolution dictated by the full system Hamiltonian—including all Zeeman, intra-, and inter-hyperfine interactions—as well as the average decay from particle loss. The stochastic Diffusion terms, in contrast, introduce the random quantum noise associated with these loss channels. This includes noise from intra-hyperfine two-body losses and correlated noise from inter-hyperfine collisions that affects both manifolds simultaneously.

By running a large ensemble of simulations of these coupled SDEs, we can reconstruct the expectation values and variances of quantum observables (like the summed comagnetometer phase $\theta^{(12)}\big)$. This method simulates the full quantum dynamics, including quantum noise, spin-mixing, and both independent and correlated loss mechanisms, providing a realistic estimate for the sensor's sensitivity.

2.4.1 Modeling Many-Body Dynamics with TWA

For this work, we used a TWA simulation code previously developed within our group. We modified the code to investigate two aspects: (1) orientation-to-alignment conversion, and (2) the equivalent magnetic sensitivity predicted by the TWA. Due to space limitations, we focus here on the latter, which is directly relevant to Sec. 4.1 and Sec. 4.2.

The code models a two-component ^{87}Rb Bose-Einstein condensate with 100,000 atoms evenly split between the $F = 1$ and $F = 2$ hyperfine states. Atoms are confined in a harmonic trap with mean frequency $\omega_{\text{trap}} = 2\pi \times 91$ Hz, defining the effective interaction volume. The system's coherent dynamics are governed by the comagnetometer SMA Hamiltonian (Eq. 7). This includes the one-body QZS, with a magnitude of $q/h = 0.89$ Hz that acts with opposite sign on the $F = 1$ and $F = 2$ manifolds. It also includes the two-body spin-exchange collisions, whose interaction strengths are calculated from the experimentally determined s-wave scattering lengths for ^{87}Rb, accounting for both intra- and inter-manifold interactions [11]. Incoherent two-body losses, both spin-dependent and spin-independent, are included with experimentally measured rates [12] [11] for collisions within $F = 2$ and between components. The system evolves according to stochastic differential equations incorporating the full Hamiltonian and loss terms (Eq. 15).

The simulation mimics a Ramsey experiment: we prepare an initial transverse coherent spin state applying a $\pi/2$ pulse to pure m_F populations, with quantum fluctuations introduced via complex Gaussian noise sampling the Wigner distribution. The system evolves for 4 seconds, and final sensitivity is computed from 200 independent trajectories. Phase noise is derived from the standard deviation of the summed comagnetometer phase.

2.4.2 TWA-Simulated Comagnetometer Sensitivity

The calculated phase noise is used to determine the Equivalent Magnetic Sensitivity from the previously derived Eq. (9). The result of this simulation, presented in Fig. 2, quantify the realistic sensitivity of the comagnetometer. We observe a big divergence between the TWA prediction (blue line) and the idealized SQL (red line). This shows that our comagnetometer is indeed shearing noise limited.

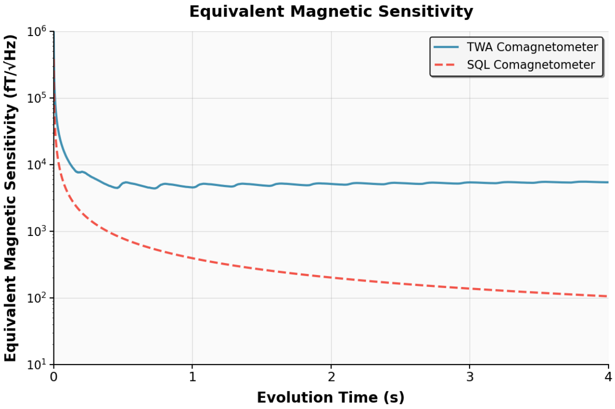

Figure 2: TWA-Simulated vs. SQL-Limited Comagnetometer Sensitivity. The plot compares the realistic sensitivity from TWA simulations (solid blue), with the idealized SQL (dashed red).

The TWA model's sensitivity floor reflects the trade-off between signal integration and dephasing. While a longer evolution time allows for greater phase accumulation from a signal, it also increases the loss of phase coherence due to particle loss and spin-mixing dynamics. This balance establishes an optimal evolution time beyond which the sensitivity no longer improves. The oscillations we see on this sensitivity floor are a direct signature of the coherent orientation-to-alignment conversion driven by the competition between the QZ effect and ferromagnetic interactions. At the coherence time of the SBEC, $t_{\text{coh}} \approx 1$ s, the minimum sensitivity reaches $4532.56\,\text{fT}/\sqrt{\text{Hz}}$. This value is used in Sec. 4 to project the sensor's scientific reach.

3 Experimental Apparatus: Design & Characterization

3.1 System Overview and Experimental Upgrades

The general experimental sequence has already been demonstrated in previous work by our group [13, 6], where a single-domain spinor Bose–Einstein condensate (SBEC) is created through magneto-optical trapping (MOT), molasses cooling, and forced evaporative cooling in a crossed optical dipole trap (ODT). The subsequent sequence, state preparation via RF and microwave pulses, coherent Larmor precession, and non-destructive Faraday-based spin readout, has also been experimentally implemented and characterized in those works. In Fig. 3, we show this second part of the protocol, which is the segment most relevant to the magnetometry application discussed here.

However, moving from a general-purpose SBEC experiment to a dedicated sensor for fundamental physics searches imposes stringent new requirements. The primary challenges are:

1. Achieving a high data-acquisition rate to allow for long-term signal averaging.
2. Creating a magnetically quiet environment while maintaining the complex optical and mechanical access required for cooling, trapping, and probing the atoms.

The upgrades described here were designed to meet these needs:

1. High-flux 2D MOT: To address the need for a high data rate, a new high-flux 2D MOT is being developed. By pre-cooling and collimating a high-flux atomic beam into the main science chamber, this upgrade will dramatically shorten the MOT loading time, reducing the overall experimental cycle time and increasing the number of measurements that can be averaged in a given period.
2. Magnetic shielding: To address the challenge of creating a magnetically quiet yet accessible environment, we are developing an integrated vacuum and magnetic shield assembly. The shield design is optimized for optical and mechanical access, and its performance is analyzed via finite element method (FEM) simulations (see Sec. 3.2).
3. In-vacuum PCB coils: Compact, UHV-compatible PCB coils are being developed to generate both the MOT quadrupole field and homogeneous bias fields. Placing them inside the chamber avoids interference with the magnetic shielding and maintains field control close to the atoms.

The experimental system is developed collaboratively within our group, with each member leading a specific component.

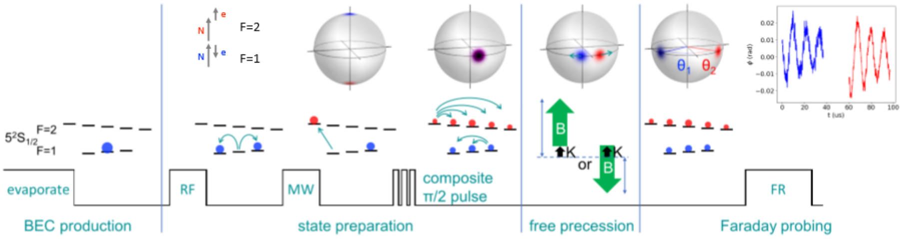

Figure 3: Schematic sequence of spinor BEC comagnetometry following condensate preparation. After the production of a single-domain SBEC, the atoms are transferred into a coherent superposition of the $F = 1$ and $F = 2$ hyperfine manifolds via a combination of RF and microwave pulses. A composite $\pi/2$ pulse then tips the spin into the transverse plane, initiating free Larmor precession in a controlled magnetic field. The spin dynamics are finally read out using non-destructive Faraday rotation probing.

3.2 Magnetic Shielding: Design and Simulation

As discussed in Sec. 2.2, the dominant noise source in our magnetometer is the ambient magnetic field and its fluctuations. The comagnetometer configuration significantly suppresses this noise. Still, we aim to further reduce residual effects using passive magnetic shielding. The comagnetometer relaxes the need for extreme shielding performance, our goal is a shielding factor of approximately 100.

3.2.1 Magnetic Shielding for Exotic Physics Searches

Before designing the experiment, we must answer a fundamental question: does the magnetic shield, while blocking ordinary magnetic fields, also suppress the exotic spin-dependent interactions we aim to detect?

The literature presents conflicting views, [14][15], but in this work, we follow the reasoning of Ref. [16], which shows that the shield's effect depends on the nature of the exotic field's coupling to Standard Model particles.

1. Nuclear-Spin Coupling: For an exotic field that couples primarily to the spins of nucleons (protons and neutrons), a standard magnetic shield made of a soft ferromagnet like µ-metal is effectively transparent. The shielding mechanism relies on the interaction of fields with the electron spins in the shield material; it, therefore, has a negligible effect on fields that do not couple to electrons.

2. Electron-Spin Coupling: For an exotic field that couples to electron spins, the shield acts as a transducer. The exotic field exerts a torque on the electron spins within the μ-metal, causing a magnetization of the shield material itself. This magnetization, in turn, generates a real, conventional magnetic field, B_{ind} , inside the shielded volume

$$B_{ind} \approx -\frac{\xi}{g\mu_B}\Upsilon \tag{16}$$

   where Υ represents the exotic field, ξ is its dimensionless coupling constant to electrons, and g is the electron g-factor.

In a single-species magnetometer, this induced field can cancel the direct torque from Υ, suppressing the signal. However, our experiment uses a comagnetometer that compares the precession of two different spin species. In this configuration, ordinary magnetic fields (including B_{ind}) are strongly suppressed by the differential measurement. This allows us to remain sensitive to exotic fields that couple differently to nuclear and electron spins, even in the presence of the shield.

3.2.2 Principles and Analytical Model

Passive magnetic shielding reduces the magnetic field inside a volume by surrounding it with a material of high magnetic permeability, μ_r. This material provides a low-reluctance path that redirects external magnetic flux lines, thereby attenuating the field within the shielded region, as defined by the shielding factor,

$$\mathrm{S} = \frac{\mathrm{B_{out}}}{\mathrm{B_{in}}}, \tag{17}$$

with B_{ext} and B_{in} the magnetic field strengths outside and inside the shield, respectively.

A. Geometry and Material Selection

We chose a spherical geometry because it is theoretically optimal for magnetic shielding. It provides a uniform magnetic reluctance path that maximizes shielding efficiency by avoiding the edge effects and local magnetic saturation found in cubic or cylindrical geometries. From a quantum sensing perspective, the spherical symmetry also minimizes electric field gradients at the cell walls, reducing systematic frequency shifts due to the coupling between the atoms' electric quadrupole moments and surrounding fields.

We select μ-metal for our shield due to its very high magnetic permeability. Although μ metal saturates at relatively low magnetic fields (around 0.75 T), our system operates at much weaker fields on the order of mG, well below saturation. Simulations with varying μ_r values confirm that μ-metal effectively meets our shielding requirements.

B. Analytical Formula

For a single, closed spherical shell of inner radius a and outer radius b, the theoretical shielding factor in a uniform DC field is given by [17]

$$S_{\mathrm{DC}} = 1 + \frac{2\,(\mu_r - 1)^2}{9\mu_r}\left[1 - \left(\frac{a}{b}\right)^3\right], \tag{18}$$

For a thin shell where $t = b - a \ll a$ and $\mu_r \gg 1$, this simplifies to

$$S_{DC} \approx 1 + \left(\frac{2}{9}\mu_r\right)\left(\frac{3t}{a}\right) = 1 + \frac{2}{3}\mu_r\frac{t}{a} \tag{19}$$

Multilayered shields significantly enhance performance. The total attenuation is approximately the product of the attenuation provided by each layer, as each successive layer encounters a pre-attenuated field. However, because our experiment involves a complex arrangement of beams for cooling, trapping, and probing atoms, we prioritize maximizing optical access and therefore focus on optimizing a single-layer shield design for now.

To confirm the validity of the analytical formulas and establish a robust simulation framework, we performed Finite Element Method (FEM) simulations using COMSOL Multiphysics. We modeled an ideal, closed spherical shell and compared its performance against the theoretical predictions across a range of material properties and geometries.

The results, shown in Fig. 4, demonstrate excellent agreement between the analytical solutions (solid lines) and the FEM simulations (data points).

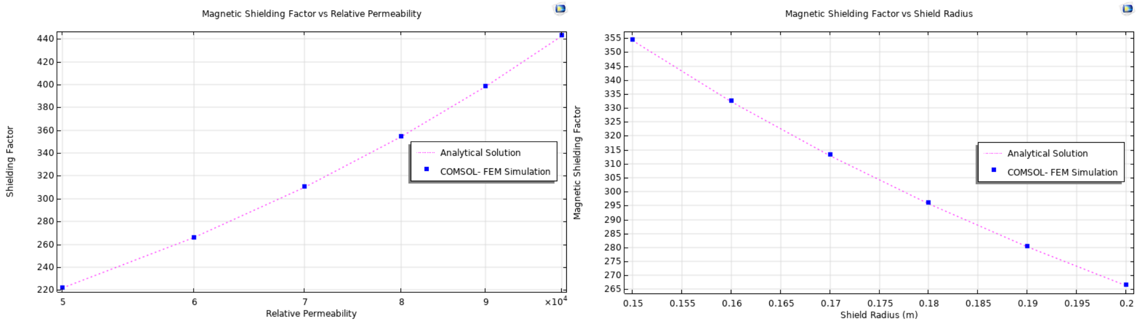

(a) Shielding factor vs relative permeability ($t = 1$ mm, $b = 150$ mm).

(b) Shielding factor vs shield radius ($t = 1$ mm, $\mu_r = 8 \times 10^4$).

Figure 4: **Validation of the FEM model against analytical solutions for an ideal spherical shield.** The plots compare the analytical solution (solid line) with results from the COMSOL FEM simulation (data points) for a single-layer spherical shield in a uniform external field of $B_0 = 1\mathrm{G}$.

3.2.3 FEM Simulations of Realistic Shield Designs

The dimensions of the final magnetic shield will be customizable depending on the size of the PCB coils. As a starting point for simulations, we use the geometry of a Kurt J. Lesker Sp1200s vacuum chamber to evaluate the overall shielding performance. This geometry currently meets our requirements in terms of size, number of openings, and aperture dimensions.

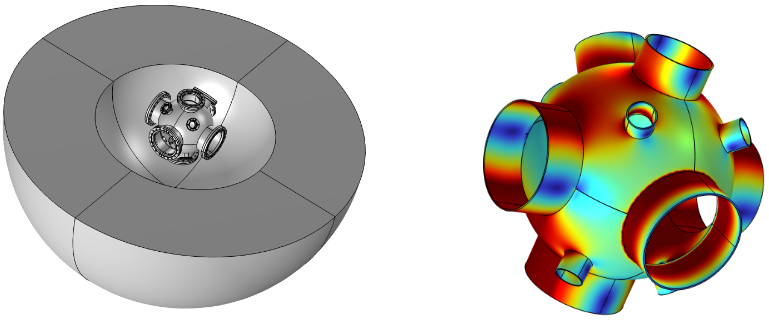

(a) The detailed CAD model of the Kurt J. Lesker Sp1200s vacuum chamber

(b) The simplified model used for simulation, where fine details have been removed to allow for computationally feasible mesh generation in COMSOL.

Figure 5: Simplification of the Shield Geometry for FEM Analysis.

As shown in Fig. 6, the simulated performance of the Sp1200s model deviates significantly from the ideal analytical prediction. While the analytical model for a perfect sphere of similar dimensions predicts a shielding factor > 400, the FEM simulation of the apertured chamber yields a factor of only ~ 80. This result demonstrates that the performance is overwhelmingly dominated by magnetic field leakage through the geometric apertures, not by the intrinsic permeability of the material. Nevertheless, this result also confirms that our design goal of $S \approx 100$ remains a realistic and appropriate target for a single-layer shield providing the necessary optical access.

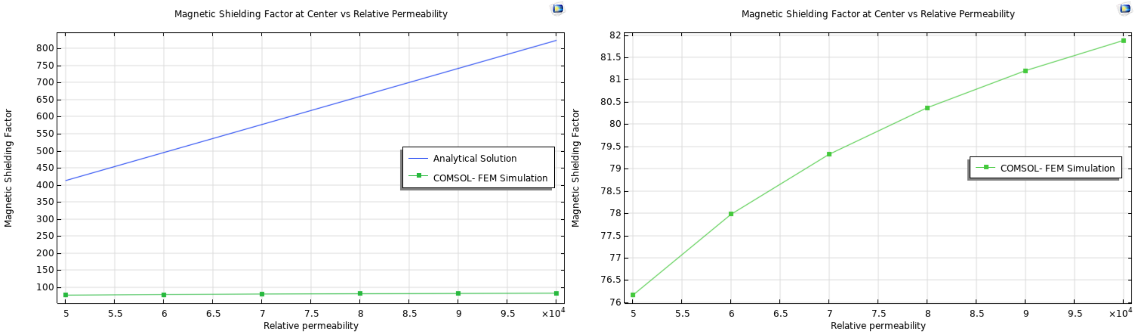

(a) Analytical vs. FEM simulation.

(b) FEM simulation

Figure 6: **FEM Simulations of magnetic shielding factor of a Sp1200s Toy Model.** The plots compare the analytical prediction for an ideal sphere (blue line) with the FEM simulation results for the apertured Sp1200s model (green dots).

3.3 Characterization of a Shot-Noise-Limited Faraday Readout System

To probe the spin state of our ultracold atomic ensemble, we employ a non-destructive measurement based on the Faraday effect. This technique uses a far-off-resonant laser beam, which passes through the atoms and experiences a polarization rotation proportional to the collective atomic spin along the probing direction. Because the light is far from any atomic resonance, photon absorption is small, allowing us to measure the spin state without significantly perturbing the atoms or heating the cloud.

At the heart of our readout system is a balanced differential photodetector (DPD). The model we use is the same one described in detail in the reference paper by Ciurana et al.[4]. As this detector had been unused for some time, the first task for this project was to remount the entire Faraday detection scheme and perform a full characterization to verify its performance.

The goal of this characterization is to map the detector's noise as a function of incident optical power. Any measurement is limited by noise, which can be modeled by the variance of the output signal:

$$\operatorname{Var}\left(V_{\text{diff}}\right) = a_0 + \eta N + a_2 N^2 \tag{20}$$

This equation separates the noise into three distinct physical sources:

1. Electronic Noise (c_0): A power-independent noise floor from the detector electronics. This sets the ultimate sensitivity limit of the instrument in darkness.
2. Shot Noise (c_1): The fundamental quantum noise arising from the discrete nature of photons, which scales linearly with photon number.
3. Technical Noise ($c_2 N^2$): Classical noise from fluctuations in the laser power itself, which dominates at high power.

Our goal is to operate in the shot-noise-limited (SNL) regime, where the shot noise term is the dominant contribution to the total noise. This ensures our measurements are limited only by fundamental quantum fluctuations.

To perform the characterization, we aligned the full optical path (already constructed by [1]). The probe beam is derived from the 780 nm repumper laser and modulated using an acousto-optic modulator (AOM) in a double-pass cat-eye configuration. This setup allows us to produce well-defined optical pulses. The modulated beam is coupled into a polarization-maintaining (PM) fiber, delivering light to the main experimental table. There, a half-wave plate (HWP) and polarizing beam splitter (PBS) act as a variable attenuator, enabling precise control over optical power while preserving polarization. The beam then enters the polarimeter stage: another HWP and PBS split the beam into orthogonal polarization components, which are directed onto the two photodiodes of the DPD via steering mirrors.

The DPD is not a simple photodiode; as described in the reference paper, its core is a Cremat CR-110 charge-sensitive preamplifier configured as a differential integrator. When we sent a relatively long optical pulse of 5 µs, we observed that a slight imbalance in power on the photodiodes resulted in a sawtooth-shaped voltage on the oscilloscope. This is the direct signature of the integrator charging during the 5 µs pulse-on time and beginning to relax during the 55 µs off-time. We found that the perfectly balanced condition, where the power on both photodiodes is equal, corresponds to the point where this sawtooth signal completely disappears into a flat line when the signal is off and some photon shot noise, when the signal is on.

Following the procedure from the reference paper[4], we recorded the detector's output for seven different optical power levels. For this characterization, we used 780 nm light from the repumper laser, pulsed by the AOM with a 5 µs pulse duration and a 60 µs period (i.e., 55 µs of off-time). For each power level, we recorded a train of 100 pulses. To calculate the signal voltage for a single pulse, we took the difference between the average voltage over 10 timesteps immediately after the pulse and the average voltage over 10 timesteps just before it. We then computed the variance of these 100 signal voltage values to obtain a single data point for our noise characterization plot. Our light source was not powerful enough to observe the technical noise regime with single pulses. To overcome this, we followed the "composite-pulse" method from the reference paper, where the signals from multiple pulses are summed in post-processing to simulate a single, higher-energy pulse.

The results of this characterization are shown in Fig. 7. The experimental data are fit to the noise model from Eq. (20), where the variance is measured in V^2.

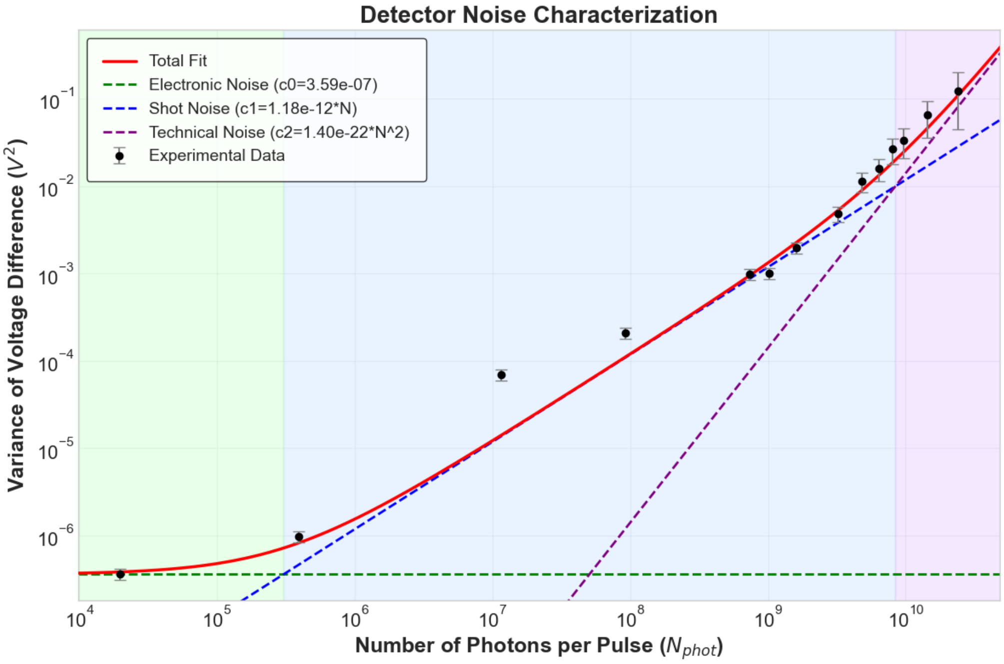

Figure 7: Characterization of detector noise. The variance of the output voltage is plotted against the number of photons per pulse (N_{phot}) on a log-log scale. Experimental data (black dots) are fitted with the model from Eq. (20) (solid red line) that sums the contributions from electronic noise (green dashed line), a linear shot noise term (blue dashed line), and a quadratic term (purple dashed line).

A fit to the data gives the following noise coefficients:

1. Electronic Noise (c_0): $(3.59 \pm 1.07) \times 10^{-7} V^2$
2. Shot Noise (c_1): $(1.18 \pm 0.25) \times 10^{-12} V^2/$ photon
3. Technical Noise (c_2) : $(1.40 \pm 1.19) \times 10^{-22} V^2/$ photon ^{2}

From these values, we determine the shot-noise-limited (SNL) operating range of the detector to be:

$$N_{\text{phot}} \in \left[\frac{c_0}{c_1}, \frac{c_1}{c_2}\right] = (3.04 \pm 1.11) \times 10^5 \text{ to } (8.41 \pm 7.34) \times 10^9 \text{ photons per pulse.} \tag{21}$$

This confirms that our detector operates within a broad SNL regime.

4 Scientific Reach: Probing for New Physics

In this chapter, we explore how the unique sensitivity of our SBEC magnetometer and comagnetometer to spin-dependent forces can be used to probe new fundamental interactions, with a particular focus on ALPs and GWs.

4.1 Search for Axion-like Dark Matter

The existence of dark matter is now supported by a wide range of astrophysical observation, from the anomalous rotation curves of galaxies [18], to gravitational lensing around massive clusters [19], and the fine-scale structure of the cosmic microwave background. Together, these phenomena point to the presence of a non-baryonic, non-luminous form of matter that accounts for roughly 85% of the total mass in the universe. However, despite its gravitational influence, the identity of this dark component still remains unknown.

Among the leading candidates for dark matter are ALPs, a class of light, weakly interacting bosons predicted by many extensions of the Standard Model. The original axion was proposed by Peccei and Quinn in the 1970s [20] as a solution to the strong CP problem in quantum chromodynamics (QCD). Although QCD allows a CP-violating term in the Lagrangian, no such violation has ever been observed. The Peccei-Quinn mechanism introduces a new global symmetry that naturally suprpesses this term, with the axion emerging as a pseudo-Goldstone boson associated with its spontaneous breaking [3].

4.1.1 Spin-Dependent Monopole-Dipole Interaction

This work focuses on the potential for axion-like particles (ALPs) to mediate new macroscopic spindependent forces. Specifically, we consider the monopole-dipole interaction described in Ref. [21], where an unpolarized particle (a "monopole") interacts with a spin-polarized particle (a "dipole") through the exchange of a virtual ALP, as illustrated in Fig. 8.

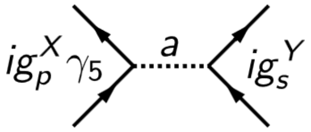

Figure 8: Feynman diagram of the monopole-dipole interaction, showing the exchange of an axion-like particle 'a' between two fermion lines (of particles X and Y) with pseudoscalar (igp) and scalar (igs) couplings.

In the non-relativistic regime, this interaction gives rise to a potential between a single unpolarized source particle (Y) at position $\mathbf{r}'$ and a single polarized target particle (X) at position $\mathbf{r}_{\text{det}}$:

$$V(\mathbf{r}) = -\frac{g_P^X g_S^Y \hbar}{4\pi mc} \hat{\sigma}_X \cdot \hat{\mathbf{r}} \left(\frac{1}{r\lambda} + \frac{1}{r^2} \right) e^{-r/\lambda} \tag{22}$$

where m is the mass of the polarized particle, $\hat{\sigma}$ is its spin, $\hat{r}$ is the unit vector from source to detector, and $\lambda = \hbar / (m_a c)$ is the range of the interaction set by the ALP mass m_a.

To understand how this microscopic potential gives rise to a macroscopic, measurable

---

[3] While broader families of ALPs arise in various theories beyond the Standard Model, such as string theory, in this work we focus on QCD axions originating from the Peccei-Quinn mechanism.

effect, we must sum the contributions from all nucleons in the source mass. The total interaction Hamiltonian, H_{ALP} is the integral of $V(r)$ over the source volume, where $\mathbf{r}$ is the vector from each source element at position $\mathbf{r'}$ to the detector. We can factor out the sensor's spin operator $\mathbf{F}$ from the integral:

$$H_{\mathrm{ALP}} = \int_{\text{source}} d^3r' n\left(r'\right) V(r) = -\hat{F} \cdot \left[\int_{\text{source}} \frac{\hbar}{2\pi m} \left|\frac{g_P g_S}{\hbar c}\right| \hat{r} \left(\frac{1}{r\lambda} + \frac{1}{r^2}\right) e^{-r/\lambda} n\left(r'\right) d^3r'\right] \tag{23}$$

This expression is now in the form of a Zeeman interaction: $H = \vec{\mu} \cdot \vec{B} = -\gamma \vec{F} \cdot \vec{B}$, where $\vec{\mu} = \gamma \vec{F}$ is the magnetic moment of the sensor atoms. By comparing the equations, we can identify the term in the brackets as the effective pseudo-magnetic field, scaled by the gyromagnatic ratio.

$$B_{\mathrm{ALP}} = \frac{\hbar}{2\pi m \gamma} \left|\frac{g_P g_S}{\hbar c}\right| \int_{\text{source}} n\left(r'\right) \hat{r} \left(\frac{1}{r\lambda} + \frac{1}{r^2}\right) e^{-r/\lambda}\, d^3r' \tag{24}$$

This integral, which we evaluate numerically, gives the final expression for the pseudo-magnetic field originated from the monopole-dipole interaction that the experiment aims to detect. Full derivation of this expression and the integral are available in Appendix **??**.

4.1.2 Sources of Monopole-Dipole Interaction

Our sensitivity calculations are based on two distinct source masses chosen to optimize the search across different interaction ranges: Earth and a laboratory Tungsten mass.

The Earth is the largest and closest available source of unpolarized nucleons. Its immense mass provides the strongest possible signal for interactions with a very long range λ from kilometers to astronomical scales.

The tungsten is chosen for its exceptional nucleon density, making it an ideal local source for probing new forces with a short interaction range ($\lambda \lesssim$ 1cm). If we place this dense mass in close proximity ($d \approx 100\mu$m) to the SBEC, we obtain a dramatic enhancement in the sensitivity to short-range mediators, which would be undetectable using a larger and more distant source like the Earth.

4.1.3 SBEC Sensitivity

A. SBEC Magnetometer

To project the experiment's discovery potential, we average the fundamental sensor noise over a realistic, long-term measurement of one week. We begin with a single-shot field noise of 72 fT, achieved over a 3.5 s measurement time. The total time for one experimental cycle is approximately 20 s [1]. Over a one-week integration period, this allows for approximately 30,240 independent measurements. Because the noise from each shot is uncorrelated, the uncertainty averages down by the square root of the number of shots. To claim a discovery, we adopt the 5σ criterion, the standard in particle physics for ensuring high statistical confidence. This results in a minimum detectable field of approximately 2.07 fT .

B. SBEC Comagnetometer (TWA Simulated)

From TWA calculations, as presented in Section 2.4, the minimum sensitivity for the comagnetometer is $4532.56\,\mathrm{fT}/\sqrt{\mathrm{Hz}}$. This value is determined at the coherence time of the comagnetometer ($t_{coh} = 1\,\mathrm{s}$) and accounts for interactions and losses. For uncorrelated measurements, this uncertainty averages down to approximately 26.06 fT after one week. Applying the same 5σ criterion, the minimum detectable field for the comagnetometer is therefore approximately 130.32 fT.

4.1.4 Results and Discussion

The projected discovery potential of our experiment is summarized in Fig. 9.

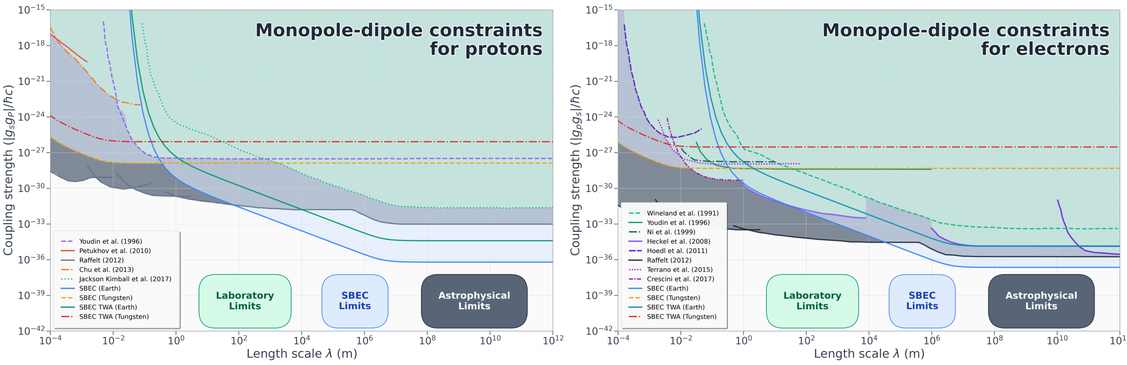

(a) Monopole-dipole constraints for protons. (b) Monopole-dipole constraints for electrons.

Figure 9: Projected constraints on the monopole-dipole coupling strength as a function of interaction range. "SBEC" refers to the magnetometer configuration; "SBEC TWA" corresponds to the simulated comagnetometer sensitivity. Constraints are derived using both the Earth (blue/green) and a nearby tungsten mass (red/orange) as unpolarized sources. The Earth is modeled as a source at a distance of 1 m from the detector, while the tungsten mass is placed at 1 μm.

Given that the comagnetometer signal is primarily sensitive to effects on proton spins, and the magnetometer to effects on electron spins, each is suited to distinct types of investigation: the comagnetometer is naturally suited for probing monopole-dipole interactions involving protons, whereas the magnetometer is better adapted to searches involving electrons. However, as previously discussed in Sec. 2.2, magnetometers are inherently limited by their extreme sensitivity to environmental magnetic fluctuations, typically overshadowing the target signal. Additionally, as discussed in Sec. 3.2, the magnetic shield itself, composed primarily of electrons, interacts strongly with electron-coupled pseudomagnetic fields, further suppressing sensitivity. Consequently, we have greater confidence in establishing robust monopole-dipole constraints for proton interactions using the comagnetometer rather than electron interactions. This understanding guides our focus and future experimental direction.

Furthermore, the selection of source material significantly influences experimental reach and sensitivity. A tungsten mass, with its exceptionally high nucleon density and ease of precise laboratory manipulation, is ideal for exploring short-range interactions comparable to the detector scale. In contrast, using Earth as a source exploits its large mass to explore long-range interactions. It is crucial to clarify that choosing between tungsten and Earth sources is not simply about achieving the best sensitivity floor; rather, different interaction ranges correspond to different masses of ALPs. By employing both tungsten and Earth sources, we strategically target complementary, previously unconstrained regions of parameter space, thereby broadening the overall reach of our constraints.

While astrophysical constraints (see Ref. [22]) appear more stringent across much of the parameter space, they are necessarily model-dependent and subject to uncertainties in, for example, stellar models. Moreover, it is possible that a "chameleon mechanism" could screen such exotic interactions in the high-density environments of astrophysical objects, potentially invalidating these bounds [23]. Thus, direct laboratory measurements still plays a crucial, comparatively less ambiguous role in the search for new physics.

4.2 Search for High-Frequency Gravitational Waves

Gravitational waves (GWs) are ripples in space and time, predicted by Albert Einstein in 1916 through his theory of General Relativity [24]. In this theory, gravity is not a force but a result of spacetime being curved by mass and energy. When massive objects like black holes accelerate or collide, they disturb this curvature and produce GWs that travel at the speed of light.

For almost a century, these waves remained a theoretical idea. This changed in 2015, when the LIGO experiment made the first direct detection from the merger of two black holes, marking the start of gravitational-wave astronomy. Since then, detectors such as Virgo, and KAGRA have observed many similar events. However, they are only sensitive to frequencies between about 10 Hz and a few kHz.

A wide and scientifically important frequency range—from the kHz to the GHz—remains unexplored [25]. This high-frequency window is thought to contain signals from exotic sources, such as primordial black hole evaporation or phase transitions in the early universe [26]. Reaching this regime requires completely new types of detectors that can sense gravitational waves at much smaller length scales.

4.2.1 Spin-Gravity Coupling in Curved Spacetime

To model how a GW interacts with the spin of a fermion in our detector, we must build upon the fundamental equations of relativistic quantum mechanics. The starting point is the Dirac equation, which describes a spin-1/2 particle in flat spacetime:

$$(i\hbar c\gamma^\mu\partial_\mu - mc^2)\psi = 0, \tag{25}$$

where ψ is the four-component Dirac spinor, γ^μ are the Dirac matrices, and the equation's solutions yield the particle's energy and momentum.

To account for electromagnetic interactions, we employ the principle of minimal coupling, where the momentum operator is modified to include the electromagnetic four-potential A_μ. This gives the familiar Dirac equation for a charged particle in an electromagnetic field:

$$\left[\gamma^\mu(i\hbar c\partial_\mu - eA_\mu) - mc^2\right]\psi = 0. \tag{26}$$

The final step is to incorporate gravity. This is achieved by generalizing the equation to a curved spacetime, where the geometry is no longer flat but is described by the metric tensor $g_{\mu\nu}$. This requires replacing the flat-space Dirac matrices γ^μ with their curved space counterparts and, most importantly, promoting the standard derivative ∂_μ to a covariant derivative, $\mathcal{D}_\mu = \partial_\mu + \Gamma_\mu$. The new term, Γ_μ, is the spin connection, which describes how the particle's spin interacts with the curvature of spacetime itself. Following this logical progression, we arrive at the fully covariant Dirac equation that accounts for both gravitational and electromagnetic interactions. From this equation, we can formulate the system's Hamiltonian[4]:

$$H = -i\left[\hbar c g_{00}\gamma^0\gamma^i\left(\partial_i + \Gamma_i + \frac{ie}{\hbar c}A_i\right) + \hbar c\Gamma_0 - ie\phi + g_{00}\gamma^0 mc^2\right]. \tag{27}$$

---

[4] Note that by taking the flat-space limit, where $g_{00}\gamma^0 \to \alpha^i$ and $g_{00}\gamma^0 \to i\beta$, we recover the standard Dirac equation in flat space,

$$i\hbar\partial_t\psi = (-i\hbar c\nabla + eA)\cdot\alpha\psi + \beta mc^2\psi - e\phi\psi.$$

This Hamiltonian, however, is fully relativistic and mixes particle (positive-energy) and antiparticle (negative-energy) solutions. To find the physically meaningful Hamiltonian for our low-energy SBEC experiment, we must systematically decouple these components. This is achieved through the Foldy-Wouthuysen (FW) transformation, a series of unitary transformations designed to eliminate the "odd" operators that mix these states. After a sequence of twelve such transformations, as detailed in Appendix D, we arrive at the final, block-diagonal, non-relativistic Hamiltonian for a particle in a weak gravitational field.

$$
\begin{aligned}
H^{\mathcal{E}}_{NR} = & \underbrace{-h_{0i}\Pi_i + \frac{1}{2mc^2}\left[\delta_{ij}\left(1-\frac{1}{2}h_{00}\right) - h_{ij}\right]\Pi_i\Pi_j}_{\text{Motion}} + \underbrace{\frac{e\hbar}{2mc}\sigma^i B_j\left[\delta_{ij}\left(1-\frac{1}{2}h_{00}-\frac{1}{2}h_{ij}\right)-\frac{1}{2}h_{ij}\right]}_{\text{Zeeman}} \\
& + \underbrace{\frac{i\hbar c}{4}\left[3\partial_i h_{0i} - \partial_0 h_{ii} - \alpha^i\alpha_j\partial_j h_{0i}\right] + \frac{\hbar^2}{16m}\partial_i^2 h_{00}}_{\text{Grav.Redshift}} - \underbrace{\frac{\hbar}{4mc}\left[3\varepsilon_{ijk}\sigma^k\partial_i h_{00} + \varepsilon_{ikl}\sigma^l\partial_i h_{jk}\right]\Pi_j}_{\text{Spin-Orbit}} \\
& + \underbrace{\frac{i\hbar}{4mc}\left(\partial_i h_{00} - \partial_i h_{jj} + \partial_j h_{ij}\right)\Pi_i + \frac{i\hbar}{4mc}\left[\partial_i h_{00} + \partial_i h_{ij}\right]\Pi_j}_{\text{small}} + \underbrace{\frac{i\hbar^2}{8m}\varepsilon_{kil}\Sigma^l\partial_k D_{ij}}_{\text{Spin-Curvature}} \\
& + \underbrace{eA_0}_{\text{EM}} + \underbrace{\left(1-\frac{1}{2}h_{00}\right)mc^2}_{\text{Rest Mass + Correction}} \quad .
\end{aligned}
\tag{28}
$$

The resulting Hamiltonian includes several gravitational couplings, but in a compact detector like our SBEC ($L \sim 10\mu$m), most are negligible. The dominant contribution is the gravitational correction to the Zeeman interaction, which appears as a GW-induced pseudomagnetic field acting on the spin. Only the magnetometer is sensitive to this signal. The comagnetometer, which cancels all B_{ext} -dependent terms, is inherently blind to it. While more susceptible to magnetic noise, the magnetometer remains the only viable configuration for detecting spin-gravity effects.

4.2.2 The Proper Detector Frame and the Effective Signal

Gravitational waves are often described in the Transverse-Traceless (TT) gauge, which assumes a freely falling frame. However, our SBEC is held by electromagnetic forces and does not meet this condition, making the TT gauge unsuitable.

Instead, we use the Proper Detector Frame (PDF) [27], which describes the lab's physical rest frame. Here, the GW appears as an oscillating tidal field across the detector's finite size, derived from the gauge-invariant Riemann tensor evaluated from the distant TT frame.

In this frame, the GW modifies the Zeeman interaction, effectively coupling the spin's magnetic moment μ to a pseudomagnetic field $B_{\text{GW}}(t)$. In the long-wavelength limit ($L \ll \lambda_{\text{GW}}$), the dominant contribution comes from the h_{00}^{PD} component, yielding:

$$
|B_{\text{GW}}|_{\text{amp}} \approx \frac{B_0 A_{GW}\omega_g^2 L^2}{4c^2} \tag{29}
$$

This field drives spin dynamics and defines the measurable signal. The full derivation and resulting strain sensitivity are presented in Appendix D.

4.2.3 Projected Sensitivity and Analysis

To estimate the strain sensitivity of our SBEC magnetometer, we equate the GW-induced pseudomagnetic signal to the magnetometer's ASD $S_B^{1/2}$. This yields the strain amplitude spectral density:

$$\sqrt{S_h\left(f_g\right)} \approx \frac{4c^2 S_B^{1/2}}{B_0 L^2 \omega_g^2} = \frac{c^2 S_B^{1/2}}{\pi^2 B_0 L^2 f_g^2} \tag{30}$$

Here, c is the speed of light, $S_B^{1/2} \approx 1.347 \times 10^{-13}$ $\mathrm{T}/\sqrt{\mathrm{Hz}}$ is the magnetic noise floor from a 72 fT singleshot sensitivity with 3.5 interrogation time, $B_0 = 120$mG is the applied field, and $L = 10\mu$m is the SBEC size. f_g is the gravitational wave frequency, and $\omega_g = 2\pi f_g$ is its angular frequency. This defines the minimum detectable GW strain as a function of frequency. The resulting sensitivity curve is shown in Fig. 10.

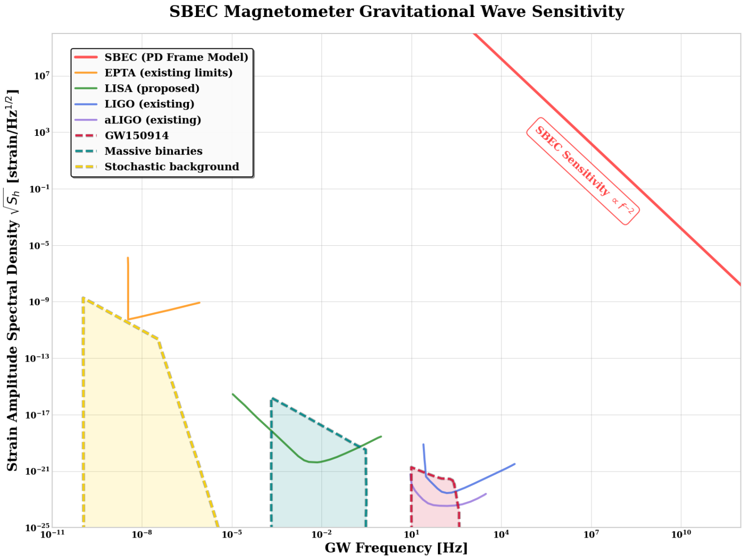

Figure 10: Projected strain sensitivity of the SBEC in the Proper Detector Frame (red), compared to existing and proposed GW detectors. Shaded regions indicate astrophysical sources.

The conclusion from Fig. 10 is clear: the projected sensitivity is many orders of magnitude worse than that of existing detectors, indicating that an SBEC magnetometer, via this interaction channel, does not have the potential to detect gravitational waves.

We also explored the possibility of resonant detection, where the Larmor frequency matches the GW frequency ($f_g = f_L$), allowing the signal to build up coherently over time. For example, at $f_g = 84\,\mathrm{kHz}$, resonance occurs with $B_0 = 120\,\mathrm{mG}$ [1], producing a pseudofield of order $10^{-26}\,\mathrm{fT}$; at $f_g = 1\,\mathrm{GHz}$, the required field rises to $B_0 \approx 1428\,\mathrm{G}$, yielding $B_{\mathrm{GW}} \sim 10^{-14}\,\mathrm{fT}$. While such a magnetic field strength is achievable in a laboratory, its effects on the BEC physics would be severe. The level structure would be completely mixed by the anomalous Zeeman effect making such a measurement impractical with the current scheme. Even with this enhancement, the signal remains far below detectable levels.

In conclusion, although the SBEC magnetometer is not competitive for GW detection, the spin-gravity formalism developed here remains valuable and could be extended to other systems—such as magnon-based detectors [26], which may offer a larger effective interaction volume and a more promising path toward high-frequency gravitational wave detection.

5 Conclusion and Outlook

This thesis presents a theoretical and simulation-based framework for employing spinor Bose-Einstein condensates (SBECs) as quantum sensors for fundamental physics. By combining theoretical modeling, realistic simulations, and experimental design elements, we explore the sensor's capabilities and outline a path toward practical implementation.

At the core of this work is a dynamical model based on the Truncated Wigner Approximation (TWA), which captures essential many-body effects including quantum noise, spin-dependent interactions, and particle loss. While not yet demonstrating sub-SQL performance, this approach enables a realistic evaluation of sensor limits under experimentally relevant conditions.

Using this framework, we examined two potential applications:

1. **ALPs:** The SBEC comagnetometer offers promising sensitivity to short-range monopole-dipole couplings, thanks to its micron-scale spatial resolution and noise rejection.

2. **GWs:** While the limited interaction volume constrains the sensor's competitiveness for high-frequency GW detection, the analysis helps clarify where this class of detectors may be effective in the future.

These findings are supported by several experimental subprojects, including finite-element simulations of a custom magnetic shield and the characterization of a shot-noise-limited Faraday polarimeter for non-destructive spin readout.

A. Outlook and Future Directions

The next phase of this research will focus on realizing a new experimental setup that integrates key elements including a high-flux 2D MOT, in-vacuum magnetic coils, and magnetic shielding. With this foundation, several research directions emerge:

1. **Characterization and Mitigation of Systematic Errors:** To ensure that any observed spin precession signals are genuinely due to new physics-and not experimental artifacts-it is essential to identify and control all sources of systematic error.

2. **Direct search for axion-like dark matter:** With both theoretical tools and experimental infrastructure in place, the SBEC comagnetometer can be used to search for ALP-mediated forces. By placing a dense tungsten mass near the condensate and modulating its position, it is possible to distinguish hypothetical signals from background noise. This experiment aims to reach the projected sensitivity estimates established in this thesis.

3. **Mitigation of interaction-induced noise:** The current sensitivity of the comagnetometer is not limited by technical noise, but by interaction-driven dephasing effects such as spin-exchange dynamics and the quadratic Zeeman effect. Addressing this limitation—either by protocol design or interaction engineering—remains a key challenge for future work.

4. **Expanding the Scientific Scope:** The SBEC comagnetometer's strong rejection of magnetic noise and high sensitivity to spin-dependent interactions make it a promising tool for additional fundamental physics searches.

In summary, this work lays the groundwork for a quantum-enhanced sensor based on spinor BECs. While challenges remain, it outlines a clear path toward experiments capable of probing physics beyond the Standard Model.

Bibliography

[1] Pau Gomez, Ferran Martin, Chiara Mazzinghi, Daniel Benedicto Orenes, Silvana Palacios, and Morgan W. Mitchell. Bose-einstein condensate comagnetometer. *Phys. Rev. Lett.*, 124:170401, Apr 2020.

[2] Samer Afach, Deniz Aybas Tumturk, Hendrik Bekker, Ben C. Buchler, Dmitry Budker, Kaleb Cervantes, Andrei Derevianko, Joshua Eby, Nataniel L. Figueroa, Ron Folman, Daniel Gavilán-Martín, Menachem Givon, Zoran D. Grujić, Hong Guo, Paul Hamilton, Morgan P. Hedges, Derek F. Jackson Kimball, Sami Khamis, Dongok Kim, Emmanuel Klinger, Abaz Kryemadhi, Xiyu Liu, Grzegorz Łukasiewicz, Hector Masia-Roig, Mikhail Padniuk, Christopher A. Palm, Sun Yool Park, Heather R. Pearson, Xiang Peng, Maxim Pospelov, Szymon Pustelny, Yossi Rosenzweig, Ophir M. Ruimi, Theo Scholtes, Perrin C. Segura, Yannis K. Semertzidis, Yun Chang Shin, Joseph A. Smiga, Yevgeny V. Stadnik, Jason E. Stalnaker, Ibrahim A. Sulai, Dhruv Tandon, Kenneth Vu, Antoine Weis, Arne Wickenbrock, Tatum Z. Wilson, Teng Wu, Wei Xiao, Yucheng Yang, Dongrui Yu, Felix Yu, Jianwei Zhang, and Yixin Zhao. What can a gnome do? search targets for the global network of optical magnetometers for exotic physics searches. *Annalen der Physik*, 536(1), July 2023.

[3] J. Stenger, S. Inouye, D. M. Stamper-Kurn, H.-J. Miesner, A. P. Chikkatur, and W. Ketterle. Spin domains in ground-state bose–einstein condensates. *Nature*, 396(6709):345–348, November 1998.

[4] F. Martin Ciurana, G. Colangelo, Robert J. Sewell, and Morgan W. Mitchell. Real-time shot-noise-limited differential photodetection for atomic quantum control. *Optics Letters*, 41(13):2946, June 2016.

[5] Silvana Palacios Alvarez, Pau Gomez, Simon Coop, Roberto Zamora-Zamora, Chiara Mazzinghi, and Morgan W. Mitchell. Single-domain bose condensate magnetometer achieves energy resolution per bandwidth below . *Proceedings of the National Academy of Sciences*, 119(6), February 2022.

[6] Silvana Palacios Alvarez. *Single-Domain Spinor Bose-Einstein Condensate.* PhD thesis, UPC, Institut de Ciències Fotòniques, 2017.

[7] M. W. Mitchell. Quantum noise and interferometry in polarized $f = 1$ spinor condensates. Unpublished notes, April 1, 2020.

[8] S. Yi, Ö. E. Müstecaplıoğlu, C. P. Sun, and L. You. Single-mode approximation in a spinor-1 atomic condensate. *Phys. Rev. A*, 66:011601, Jul 2002.

[9] S. M. Rochester and D. Budker. Atomic polarization visualized. *American Journal of Physics*, 69(4):450–454, 04 2001.

[10] Dmitry Budker and Mikhail G. Kozlov. Sensing: Equation one, 2020.

[11] Pau Gomez, Chiara Mazzinghi, Ferran Martin, Simon Coop, Silvana Palacios, and Morgan W. Mitchell. Interferometric measurement of interhyperfine scattering lengths in ^{87}Rb. *Phys. Rev. A*, 100:032704, Sep 2019.

[12] M. Egorov, B. Opanchuk, P. Drummond, B. V. Hall, P. Hannaford, and A. I. Sidorov. Measurement of s-wave scattering lengths in a two-component bose-einstein condensate. *Phys. Rev. A*, 87:053614, May 2013.

[13] Pau Gómez Kabelka. *Spinor Bose-Einstein comagnetometer and interhyperfine interactions in 87Rb.* PhD thesis, UPC, Institut de Ciències Fotòniques, Sep 2021.

[14] T. C. P. Chui and Wei-Tou Ni. Experimental search for an anomalous spin-spin interaction between electrons. *Phys. Rev. Lett.*, 71:3247–3250, Nov 1993.

[15] V. F. Bobrakov, Yu. V. Borisov, M. S. Lasakov, A. P. Serebrov, R. R. Tal'daev, and

A. S. Trofimova. *Pis'ma Zh. Eksp. Teor. Fiz.*, 53:283, 1991. [JETP Lett. **53**, 294 (1991)].

[16] D. F. Jackson Kimball, J. Dudley, Y. Li, S. Thulasi, S. Pustelny, D. Budker, and M. Zolotorev. Magnetic shielding and exotic spin-dependent interactions. *Phys. Rev. D*, 94:082005, Oct 2016.

[17] Alan K. Thomas. Magnetic shielded enclosure design in the dc and vlf region. *IEEE Transactions on Electromagnetic Compatibility*, EMC-10(1):142–152, 1968.

[18] Massimo Persic, Paolo Salucci, and Fulvio Stel. The Universal rotation curve of spiral galaxies: 1. The Dark matter connection. *Mon. Not. Roy. Astron. Soc.*, 281:27, 1996.

[19] Tristan Faber and Matt Visser. Combining rotation curves and gravitational lensing: how to measure the equation of state of dark matter in the galactic halo. *Monthly Notices of the Royal Astronomical Society*, 372(1):136–142, 09 2006.

[20] R. D. Peccei and Helen R. Quinn. CP conservation in the presence of pseudoparticles. *Phys. Rev. Lett.*, 38:1440–1443, Jun 1977.

[21] J. E. Moody and Frank Wilczek. New macroscopic forces? *Phys. Rev. D*, 30:130–138, Jul 1984.

[22] Georg Raffelt. Limits on a *cp*-violating scalar axion-nucleon interaction. *Phys. Rev. D*, 86:015001, Jul 2012.

[23] Derek F. Jackson Kimball, Jordan Dudley, Yan Li, Dilan Patel, and Julian Valdez. Constraints on long-range spin-gravity and monopole-dipole couplings of the proton. *Physical Review D*, 96(7), October 2017.

[24] Albert Einstein. Näherungsweise Integration der Feldgleichungen der Gravitation. *Sitzungsberichte der Königlich Preussischen Akademie der Wissenschaften*, pages 688–696, January 1916.

[25] Nancy Aggarwal, Odylio D. Aguiar, Andreas Bauswein, Giancarlo Cella, Sebastian Clesse, Adrian Michael Cruise, Valerie Domcke, Daniel G. Figueroa, Andrew Geraci, Maxim Goryachev, Hartmut Grote, Mark Hindmarsh, Francesco Muia, Nikhil Mukund, David Ottaway, Marco Peloso, Fernando Quevedo, Angelo Ricciardone, Jessica Steinlechner, Sebastian Steinlechner, Sichun Sun, Michael E. Tobar, Francisco Torrenti, Caner Ünal, and Graham White. Challenges and opportunities of gravitational-wave searches at mhz to ghz frequencies. *Living Reviews in Relativity*, 24(1), December 2021.

[26] Asuka Ito and Jiro Soda. A formalism for magnon gravitational wave detectors. *The European Physical Journal C*, 80(6), June 2020.

[27] Asher Berlin, Diego Blas, Raffaele Tito D'Agnolo, Sebastian A.R. Ellis, Roni Harnik, Yonatan Kahn, and Jan Schütte-Engel. Detecting high-frequency gravitational waves with microwave cavities. *Physical Review D*, 105(11), June 2022.

[28] James D. Bjorken and Sidney D. Drell. *Relativistic Quantum Mechanics.* McGraw-Hill, New York, 1964.

A The Spinor BEC Comagnetometer Hamiltonian

This appendix provides the detailed expressions for the SMA Hamiltonian for the ^{87}Rb $F = 1$ and $F = 2$ comagnetometer, as used in the TWA simulations in this work. The expressions are based on the formalism described in [1] [11] . The total energy of the system, which acts as the Hamiltonian, is the sum of three components:

$$H_{SMA} = E^{(1)} + E^{(2)} + \overline{E^{(12)}} \tag{31}$$

A. F=1 Intra-hyperfine Energy

The energy of the $f = 1$ manifold is given by[1][11]:

$$E^{(1)} = \sum_{m=-1,0,1} \left(p^{(1)}m + q^{(1)}m^2\right) \left|\xi_m^{(1)}\right|^2 + \frac{1}{2V_{eff}} g_1^{(1)} \mathbf{F}^{(1)} \cdot \mathbf{F}^{(1)} \tag{32}$$

where $p^{(1)}$ and $q^{(1)}$ are the linear and quadratic Zeeman shift coefficients, V_{eff} is the effective interaction volume, $g_1^{(1)}$ is the spin-dependent interaction coefficient, and $\mathbf{F}^{(1)}$ is the mean spin vector for the $f = 1$ manifold.

B. F=2 Intra-hyperfine Energy

The energy of the $f = 2$ manifold includes an additional spin-singlet pairing term, $\left|A_0^{(2)}\right|^2$ [1][11]:

$$E^{(2)} = \sum_{m=-2,\ldots,2} \left(p^{(2)}m + q^{(2)}m^2\right) \left|\xi_m^{(2)}\right|^2 + \frac{1}{2V_{eff}} \left(g_1^{(2)} \mathbf{F}^{(2)} \cdot \mathbf{F}^{(2)} + g_2^{(2)} \left|A_0^{(2)}\right|^2\right) \tag{33}$$

where

$$A_0^{(2)} \equiv \frac{1}{\sqrt{5}} \left(2\xi_2^{(2)}\xi_{-2}^{(2)} - 2\xi_1^{(2)}\xi_{-1}^{(2)} + \xi_0^{(2)}\xi_0^{(2)}\right). \tag{34}$$

C. Inter-hyperfine Interaction Energy

The energy describing the interaction between the two manifolds, under the rotating-wave approximation, is:

$$\overline{E^{(12)}} = \frac{1}{V_{eff}} \left(g_1^{(12)} F_z^{(1)} F_z^{(2)} + g_2^{(12)} \overline{P_1^{(12)}}\right) \tag{35}$$

The term $\overline{P_1^{(12)}}$ contains complex spin-exchange dynamics detailed in. [1][11].

D. Interaction Coefficients

The interaction coefficients $g_c^{(\mathcal{F})}$ for intra-hyperfine ($\mathcal{F} = 1, 2$) and inter-hyperfine (

$\mathcal{F} = 12$) scattering are defined by the s-wave scattering lengths $a_c^{(\mathcal{F})}$ [11] :

$$
\begin{aligned}
g_0^{(1)} &= \frac{4\pi\hbar^2}{M} \frac{a_0^{(1)} + 2a_2^{(1)}}{3} \\
g_1^{(1)} &= \frac{4\pi\hbar^2}{M} \frac{a_2^{(1)} - a_0^{(1)}}{3} \\
g_1^{(2)} &= \frac{4\pi\hbar^2}{M} \frac{a_4^{(2)} - a_2^{(2)}}{7} \\
g_2^{(2)} &= \frac{4\pi\hbar^2}{M} \frac{7a_0^{(2)} - 10a_2^{(2)} + 3a_4^{(2)}}{7} \\
g_0^{(12)} &= \frac{4\pi\hbar^2}{M} \frac{2a_2^{(12)} + a_3^{(12)}}{3} \\
g_1^{(12)} &= \frac{4\pi\hbar^2}{M} \frac{a_3^{(12)} - a_2^{(12)}}{3} \\
g_2^{(12)} &= \frac{4\pi\hbar^2}{M} \frac{3a_1^{(12)} - 5a_2^{(12)} + 2a_3^{(12)}}{3}
\end{aligned}
\tag{36}
$$

B Derivation of Sensitivity Equations

B.1 SQL

The starting point is the Heisenberg uncertainty principle for two non-commuting spin operators. For a spin system prepared with a well-defined orientation along the x-axis, the spin components in the y and z directions are fundamentally uncertain. This is expressed by the commutation relation:

$$\left[\hat{J}_y, \hat{J}_z\right] = i\hbar\hat{J}_x \tag{37}$$

This leads to an uncertainty relation for their standard deviations (ΔJ_y and ΔJ_z)

$$\Delta J_y \cdot \Delta J_z \geq \frac{\hbar}{2}|\langle\hat{J}_x\rangle| \tag{38}$$

When a system of N atoms with spin F is prepared in a coherent spin state polarized along the x-axis, the total spin projection is $\left\langle\hat{J}_x\right\rangle = N\hbar F$. For such a state, the uncertainties in the transverse spin components are equal, and at the quantum limit, they are given by:

$$\Delta J_y = \Delta J_z = \sqrt{\frac{\hbar^2 NF}{2}} = \hbar\sqrt{\frac{NF}{2}} \tag{39}$$

The phase angle θ of the spin vector is determined by the relationship between the transverse spin component $\left\langle\hat{J}_y\right\rangle$ and the total spin length $|J| = N\hbar F$. For small angles, this can be approximated as $\theta \approx \frac{\langle\hat{J}_y\rangle}{|J|}$. The uncertainty in this phase angle, $\delta\theta$, is therefore:

$$\delta\theta \approx \frac{\Delta J_y}{|J|} = \frac{\hbar\sqrt{NF/2}}{N\hbar F} = \frac{1}{\sqrt{2NF}} \tag{40}$$

This is the well-known result for the SQL of phase estimation for a single ensemble of N atoms (magnetometer).

Our comagnetometer is not a single ensemble, but two independent ensembles ($f = 1$ and $f = 2$) that are measured separately. The total noise in our measurement is the combination of the noise from each.

1. Atom Distribution: The total number of atoms, N, is split approximately equally between the two manifolds. So, $N_1 \approx N/2$ and $N_2 \approx N/2$.
2. Noise from Each Manifold: Applying the SQL result from step 2, the phase noise for each individual manifold is:
   (a) $\delta\theta^{(1)}_{SQL} \approx \frac{1}{\sqrt{2N_1F_1}} = \frac{1}{\sqrt{2(N/2)\cdot 1}} = \frac{1}{\sqrt{N}}$
   (b) $\delta\theta^{(2)}_{SQL} \approx \frac{1}{\sqrt{2N_2F_2}} = \frac{1}{\sqrt{2(N/2)\cdot 2}} = \frac{1}{\sqrt{2N}}$
3. Total Noise: The total noise, σ_{SQL}, is the quadrature sum of the independent noise sources from each measurement:

$$\begin{aligned} \sigma_{SQL} &= \sqrt{\left(\delta\theta^{(1)}_{SQL}\right)^2 + \left(\delta\theta^{(2)}_{SQL}\right)^2} \\ \sigma_{SQL} &\approx \sqrt{\left(\frac{1}{\sqrt{N}}\right)^2 + \left(\frac{1}{\sqrt{2N}}\right)^2} = \sqrt{\frac{1}{N} + \frac{1}{2N}} = \sqrt{\frac{3}{2N}} \end{aligned} \tag{41}$$

The general expression for the equivalent magnetic sensitivity (for the comagnetometer) is given by

$$S_B^{(12)} = \frac{\sqrt{t_{cyc}}}{\gamma_0 t_{coh}} \sigma_{\text{ensemble}} \tag{42}$$

where σ_{ensemble} is the total phase noise of the measurement:

$$\sigma_{\text{ensemble}}(t) = \frac{\sigma_{\text{single}}\ (t)}{\sqrt{N(t)}} \tag{43}$$

To find the SQL for sensitivity, we substitute the ensemble noise term, σ_{ensemble}, with the SQL phase noise we derived, $\sigma_{SQL} = \sqrt{3/2N}$

$$\text{SQL Sensitivity } = \frac{\sqrt{t_{cyc}}}{\gamma_0 t_{coh}} \left(\sqrt{\frac{3}{2N}} \right) \tag{44}$$

This is the theoretical best-case sensitivity for the comagnetometer, where performance is limited only by the fundamental quantum projection noise of the N atoms.

C Derivation of the ALP-Induced Pseudomagnetic Field

C.1 Hamiltonian

We choose this convention:

$$V(\mathbf{r}) = -\frac{g_P^i g_S^j \hbar}{4\pi m_i c}\hat{\sigma}_i \cdot \hat{\mathbf{r}}\left(\frac{1}{r\lambda}+\frac{1}{r^2}\right)e^{-r/\lambda} \tag{45}$$

with

1. g_p: Pseudo-scalar coupling constant, describing the interaction between the ALPs and the Test mass.
2. g_s: Scalar coupling constant, describing the interaction between the ALPs and the source mass.
3. $\hat{\sigma}_i$: pauli matrices.
$$\hat{\sigma} = \hat{S}\frac{2}{\hbar} = \hat{F}\frac{2}{\hbar} \tag{46}$$
4. $\mathbf{r}$: position vector from the source particle to the spin particle.
5. $\lambda = \hbar/(m_a c)$: Interaction range or reduced Compton Wavelength of the mediating ALPs with mass m_a.

The total interaction Hamiltonian H_{ALP} for a single detector spin $\mathbf{F}$ interacting with a macroscopic source object (composed of nucleons) is obtained by summing (integrating) the potential $V(r)$ over all source particles. Let the detector spin be located at r_{det} and a source element with nucleon number density $n\left(r'\right)$ be at r'. The vector from the source element to the detector is $r = r_{\text{det}} - r'$.

$$H_{ALP} = \int_{\text{source}} d^3r' n\left(r'\right) V(r) \tag{47}$$

The total Hamiltonian is:

$$H_{ALP} = \int_{\text{source}} d^3r' n\left(r'\right)\left[-\frac{g_P g_S}{2\pi m_i c}(\hat{F}\cdot\hat{r})\left(\frac{1}{r\lambda}+\frac{1}{r^2}\right)e^{-r/\lambda}\right] \tag{48}$$

Using the nucleon density $\rho\left(r'\right) = n\left(r'\right) m_n$ (with $n(r')$ the nucleon number density) (since $m_p \approx 1.6726 \times 10^{-27}$ kg $\approx m_n \approx 1.6749 \times 10^{-27}$kg, with a difference of only 0.14%, thus, we use m_p for the average nucleon mass to simplify equations):

$$H_{ALP} = -\hat{F}\cdot\left[\int_{\text{source}} d^3r' \frac{\rho\left(r'\right)}{m_p}\frac{g_P g_S}{2\pi m_i c}\hat{r}\left(\frac{1}{r\lambda}+\frac{1}{r^2}\right)e^{-r/\lambda}\right] \tag{49}$$

We want to express this in the form of an effective field $H_{md} = -\gamma F \cdot B_{md}$. Therefore:

$$B_{ALP} = \frac{g_P g_S}{2\pi\gamma m_i m_p c}\int_{\text{source}} d^3r' \rho\left(r'\right)\hat{r}\left(\frac{1}{r\lambda}+\frac{1}{r^2}\right)e^{-r/\lambda} \tag{50}$$

Let's define the vector integral as:

$$I(\lambda) = \int_{\text{source}} d^3r' \rho\left(r'\right)\hat{r}\left(\frac{1}{r\lambda}+\frac{1}{r^2}\right)e^{-r/\lambda} \tag{51}$$

where $r = r_{\text{det}} - r'$ is the vector from the source element d^3r' to the detector. The effective pseudo-magnetic field is then:

$$B_{\text{ALP}} = \frac{g_P g_S}{2\pi\gamma m_i m_p c} I(\lambda) \tag{52}$$

This pseudo-magnetic field causes a shift in the Larmor frequency:

$$\Delta\omega = \gamma B_{\text{ALP}} = \gamma \left| \frac{g_P g_S}{2\pi\gamma m_p m_i c} I(\lambda) \right| = \left| \frac{g_P g_S}{2\pi m_p m_i c} \right| |I(\lambda)| \tag{53}$$

The detection threshold for the monopole-dipole interaction is met when the pseudo-magnetic field B_{ALP} equals the minimum detectable field. Therefore:

$$\left| \frac{g_P g_S}{2\pi\gamma m_p m_i c} I(\lambda) \right| = B_{\min} \tag{54}$$

Thus,

$$\left| \frac{g_P g_S}{\hbar c} \right|_{\min} = \frac{2\pi\gamma m_p m_i B_{\min}}{\hbar |I(\lambda)|} \tag{55}$$

C.2 Integral for Sources

We need to compute $I(\lambda) = \int_{\text{source}} d^3r' \rho(r') \hat{r} \left(\frac{1}{r\lambda} + \frac{1}{r^2}\right) e^{-r/\lambda}$, where $r = r_{\text{det}} - r'$. Due to the symmetry of the sources (sphere, cylinder centered below the detector), the net field B_{ALP} and thus $I(\lambda)$ will point vertically. Let the detector be at $r_{\text{det}} = (0, 0, D)$ relative to the center of the source (or a reference point in the source). A source point is $r'.r = r_{\text{det}} - r'$. The integral will have only a z-component.

$$\begin{aligned} I(\lambda) &= \hat{z} I_z(\lambda) \\ I_z(\lambda) &= \int_{\text{source}} dV' \rho(r') (\hat{r} \cdot \hat{z}) \left(\frac{1}{r\lambda} + \frac{1}{r^2}\right) e^{-r/\lambda} \end{aligned} \tag{56}$$

Let's place the detector at the origin $r_{\text{det}} = 0$. Source element at r'. Then $r = -r', r = r', \hat{r} = -\hat{r}'$.

$$I(\lambda) = \int_{\text{source}} dV' \rho(r') (-\hat{r}') \left(\frac{1}{r'\lambda} + \frac{1}{r'^2}\right) e^{-r'/\lambda} \tag{57}$$

Again, by symmetry, if the source is below the origin, the integral points in $-\hat{z}$.

$$\begin{aligned} I(\lambda) &= -\hat{z} \int_{\text{source}} dV' \rho(r') (\hat{r}' \cdot \hat{z}) \left(\frac{1}{r'\lambda} + \frac{1}{r'^2}\right) e^{-r'/\lambda} \\ I_z(\lambda) &= \int_{\text{source}} dV' \rho(r') \frac{z'}{r'} \left(\frac{1}{r'\lambda} + \frac{1}{r'^2}\right) e^{-r'/\lambda} \end{aligned} \tag{58}$$

Note: The sign depends on the coordinate system choice. Let's use the setup where the detector is at $z = D$ and the source is centered at the origin. Then $r = (0, 0, D) - r'$, and $\hat{r}_z = (D - z')/r$.

$$I_z(\lambda) = \int_{\text{source}} dV' \rho(r') \frac{D - z'}{r} \left(\frac{1}{r\lambda} + \frac{1}{r^2}\right) e^{-r/\lambda} \tag{59}$$

where $r = |r_{\text{det}} - r'|$.

A. Earth

We model the Earth centered at the origin, and the detector (SBEC) at $D = R_E + 1\,\mathrm{m}$. Using spherical coordinates:

$$\begin{aligned} \mathbf{r}' &= (r'\sin\theta'\cos\phi', r'\sin\theta'\sin\phi', r'\cos\theta'), \\ dV' &= r'^2 dr'\sin\theta' d\theta' d\phi', \\ r &= \sqrt{r'^2 + D^2 - 2Dr'\cos\theta}, \end{aligned} \tag{60}$$

the integral becomes:

$$I_z(\lambda) = \rho_E \int_0^{R_E} dr' r'^2 \int_0^{\pi} d\theta' \sin\theta' \int_0^{2\pi} d\phi' \frac{D - r'\cos\theta'}{r} \left(\frac{1}{r\lambda} + \frac{1}{r^2}\right) e^{-r/\lambda} \tag{61}$$

The integral $\int d\phi'$ gives 2π. Let $u = \cos\theta', du = -\sin\theta' d\theta'$. Limits $u = 1$ to $u = -1$.

$$I_z(\lambda) = 2\pi\rho_E \int_0^{R_E} dr' r'^2 \underbrace{\int_{-1}^{1} du \frac{D - r'u}{r} \left(\frac{1}{r\lambda} + \frac{1}{r^2}\right) e^{-r/\lambda}}_{\text{Let's call this } K(r')} \tag{62}$$

We now change variable from u to r in $K(r')$

1. From $r^2 = r'^2 + D^2 - 2Dr'u$, we get $2rdr = 2Dr'du \Longrightarrow du = \frac{rdr}{Dr'}$.
2. The limits $u = -1 \Longrightarrow r = D + r'$ and $u = 1 \Longrightarrow r = |D - r'| = D - r'$ (since $D = R_E + 1 > R_E \geq r'$).
3. We also found $\frac{D - r'u}{r} = \frac{D^2 - r'^2 + r^2}{2Dr}$.

Substituting these into the integral $K\left(r'\right)$:

$$K\left(r'\right) = \int_{D-r'}^{D+r'} \left(\frac{rdr}{Dr'}\right) \left(\frac{D^2 - r^2 + r^2}{2Dr}\right) \left(\frac{1}{r\lambda} + \frac{1}{r^2}\right) e^{-r/\lambda} \tag{63}$$

$$K\left(r'\right) = \frac{1}{2D^2 r'} \int_{D-r'}^{D+r'} dr \left(D^2 - r'^2 + r^2\right) \left(\frac{1}{r\lambda} + \frac{1}{r^2}\right) e^{-r/\lambda} \tag{64}$$

Let the integrand be $f(r) = \left(D^2 - r'^2 + r^2\right)\left(\frac{1}{r\lambda} + \frac{1}{r^2}\right) e^{-r/\lambda}$. We can expand this:

$$\begin{aligned} f(r) &= \left(\frac{D^2 - r'^2}{r\lambda} + \frac{D^2 - r'^2}{r^2} + \frac{r^2}{r\lambda} + \frac{r^2}{r^2}\right) e^{-r/\lambda} \\ &= \left(\frac{D^2 - r'^2}{\lambda r} + \frac{D^2 - r'^2}{r^2} + \frac{r}{\lambda} + 1\right) e^{-r/\lambda} \end{aligned} \tag{65}$$

Let's find the indefinite integral $\int f(r) dr$. We use the following standard integrals (where $a = 1/\lambda$):

1. $\int e^{-ar} dr = -\frac{1}{a} e^{-ar} = -\lambda e^{-r/\lambda}$
2. $\int r e^{-ar} dr = -\frac{e^{-ar}}{a^2}(ar + 1) = -\lambda e^{-r/\lambda}(r/\lambda + 1) = -e^{-r/\lambda}(r + \lambda)$
3. $\int \frac{e^{-ar}}{r^2} dr = -\frac{e^{-ar}}{r} - a\int \frac{e^{-ar}}{r} dr = -\frac{e^{-ar}}{r} - \frac{1}{\lambda} E_1(r/\lambda)$ (using IBP: $u = e^{-ar}, dv = dr/r^2$)

4. $\int \frac{e^{-ar}}{r} dr = E_1(ar) = E_1(r/\lambda)$ (where E_1 is the exponential integral)

Combining these for our $\int f(r)dr$:

$$\begin{aligned}\int f(r)dr &= \frac{D^2 - r'^2}{\lambda} \int \frac{e^{-r/\lambda}}{r} dr + \left(D^2 - r'^2\right) \int \frac{e^{-r/\lambda}}{r^2} dr + \frac{1}{\lambda} \int r e^{-r/\lambda} dr + \int e^{-r/\lambda} dr \\ &= \frac{D^2 - r'^2}{\lambda} E_1(r/\lambda) + \left(D^2 - r'^2\right) \left[-\frac{e^{-r/\lambda}}{r} - \frac{1}{\lambda} E_1(r/\lambda) \right] + \left[-e^{-r/\lambda}(r+\lambda) \right] + \left[-\lambda e^{-r/\lambda} \right]\end{aligned} \tag{66}$$

Simplifying by cancelling the E_1 terms:

$$\begin{aligned}\int f(r)dr &= \frac{D^2 - r'^2}{\lambda} E_1 - \frac{D^2 - r'^2}{r} e^{-r/\lambda} - \frac{D^2 - r'^2}{\lambda} E_1 - (r+\lambda) e^{-r/\lambda} - \lambda e^{-r/\lambda} \\ &= -\frac{D^2 - r'^2}{r} e^{-r/\lambda} - (r + 2\lambda) e^{-r/\lambda} \\ &= -\left[\frac{D^2 - r'^2 + r(r+2\lambda)}{r} \right] e^{-r/\lambda} \\ &= -\left[\frac{D^2 - r'^2 + r^2 + 2\lambda r}{r} \right] e^{-r/\lambda}\end{aligned} \tag{67}$$

Let $G(r) = -\left[\frac{D^2 - r'^2 + r^2 + 2\lambda r}{r}\right] e^{-r/\lambda}$. We need $G(D+r') - G(D-r')$.

$$\begin{aligned}G(D+r') &= -\left[\frac{D^2 - r'^2 + (D+r')^2 + 2\lambda (D+r')}{D+r'} \right] e^{-(D+r')/\lambda} \\ &= -\left[\frac{D^2 - r'^2 + D^2 + 2Dr' + r'^2 + 2\lambda (D+r')}{D+r'} \right] e^{-(D+r')/\lambda} \\ &= -\left[\frac{2D^2 + 2Dr' + 2\lambda (D+r')}{D+r'} \right] e^{-(D+r')/\lambda} \\ &= -\left[\frac{2D(D+r') + 2\lambda (D+r')}{D+r'} \right] e^{-(D+r')/\lambda} \\ &= -[2D + 2\lambda] e^{-(D+r')/\lambda}\end{aligned} \tag{68}$$

$$\begin{aligned}G(D-r') &= -\left[\frac{D^2 - r'^2 + (D-r')^2 + 2\lambda (D-r')}{D-r'} \right] e^{-(D-r')/\lambda} \\ &= -\left[\frac{D^2 - r'^2 + D^2 - 2Dr' + r'^2 + 2\lambda (D-r')}{D-r'} \right] e^{-(D-r')/\lambda} \\ &= -\left[\frac{2D^2 - 2Dr' + 2\lambda (D-r')}{D-r'} \right] e^{-(D-r')/\lambda} \\ &= -\left[\frac{2D(D-r') + 2\lambda (D-r')}{D-r'} \right] e^{-(D-r')/\lambda} \\ &= -[2D + 2\lambda] e^{-(D-r')/\lambda}\end{aligned} \tag{69}$$

So,

$$\begin{aligned}G(D+r') - G(D-r') &= -2(D+\lambda) e^{-(D+r')/\lambda} - \left(-2(D+\lambda) e^{-(D-r')/\lambda} \right) \\ &= 2(D+\lambda) \left[e^{-(D-r')/\lambda} - e^{-(D+r')/\lambda} \right] \\ &= 2(D+\lambda) e^{-D/\lambda} \left[e^{r'/\lambda} - e^{-r'/\lambda} \right] \\ &= 4(D+\lambda) e^{-D/\lambda} \sinh(r'/\lambda)\end{aligned} \tag{70}$$

And

$$K\left(r'\right)=\frac{2(D+\lambda)}{D^2 r'} e^{-D/\lambda} \sinh\left(r'/\lambda\right) \tag{71}$$

Now we integrate over r' :

$$\begin{aligned} I_z(\lambda) &= 2\pi\rho_E \int_0^{R_E} dr' r'^2 K\left(r'\right) \\ &= 2\pi\rho_E \int_0^{R_E} dr' r'^2 \left[\frac{2(D+\lambda)}{D^2 r'} e^{-D/\lambda} \sinh\left(r'/\lambda\right)\right] \end{aligned} \tag{72}$$

This gives:

$$I_z(\lambda)=\frac{4\pi\rho_E\lambda(D+\lambda)}{D^2} e^{-D/\lambda}\left[R_E \cosh\left(R_E/\lambda\right)-\lambda \sinh\left(R_E/\lambda\right)\right] \tag{73}$$

B. Earth Limit

We start with the general integral for $I_z(\lambda)$ for a source centered at the origin and the detector at $(0,0,D)$:

$$I_z(\lambda)=\int_{\text{source}} dV' \rho\left(r'\right) \frac{D-z'}{r}\left(\frac{1}{r\lambda}+\frac{1}{r^2}\right) e^{-r/\lambda} \tag{74}$$

where $r=\sqrt{\rho'^2+\left(D-z'\right)^2}$ is the distance from a source element at r' to the detector, and D is the z-coordinate of the detector. For Earth, $D=D_E=R_E+1m$.

As $\lambda \rightarrow \infty$:

1. The exponential term $e^{-r/\lambda} \rightarrow e^0=1$.
2. The term $\frac{1}{r\lambda} \rightarrow 0$. The integral then simplifies to:

$$I_z(\lambda \rightarrow \infty) \approx \int_{\text{source}} dV' \rho\left(r'\right) \frac{D-z'}{r^3} \tag{75}$$

For a spherical source centered at the origin, the volume element is $dV'=r'^2 dr' \sin\theta' d\theta' d\phi'$. A source point r' in Cartesian coordinates is $(r'\sin\theta'\cos\phi', r'\sin\theta'\sin\phi', r'\cos\theta')$. The detector is at $(0,0,D)$. The distance r from the source element r' to the detector is $r=$

$$\sqrt{\left(r'\sin\theta'\cos\phi'-0\right)^2+\left(r'\sin\theta'\sin\phi'-0\right)^2+\left(r'\cos\theta'-D\right)^2}. \tag{76}$$

Simplifying this

$$\begin{aligned} r &= \sqrt{r'^2\sin^2\theta'\cos^2\phi'+r'^2\sin^2\theta'\sin^2\phi'+\left(r'\cos\theta'-D\right)^2} \\ &= \sqrt{r'^2\sin^2\theta'+\left(r'\cos\theta'-D\right)^2} \\ &= \sqrt{r'^2\sin^2\theta'+r'^2\cos^2\theta'-2Dr'\cos\theta'+D^2} \\ &= \sqrt{r'^2+D^2-2Dr'\cos\theta'}. \end{aligned} \tag{77}$$

The term $(D-z')$ in the numerator is $D-r'\cos\theta'$. Now, let's substitute these into the integral:

$$I_z(\lambda \rightarrow \infty)=\int_0^{2\pi} d\phi' \int_0^{\pi} d\theta' \sin\theta' \int_0^{R_E} dr' r'^2 \rho_E \frac{D-r'\cos\theta'}{\left(r'^2+D^2-2Dr'\cos\theta'\right)^{3/2}} \tag{78}$$

Due to azimuthal symmetry, the integral over ϕ' gives 2π :

$$I_z(\lambda \to \infty) = 2\pi\rho_E \int_0^{R_E} dr' r'^2 \int_0^{\pi} d\theta' \sin\theta' \frac{D - r'\cos\theta'}{\left(r'^2 + D^2 - 2Dr'\cos\theta'\right)^{3/2}} \tag{79}$$

Let $u = \cos\theta'$. Then $du = -\sin\theta' d\theta'$. When $\theta' = 0, u = 1$. When $\theta' = \pi, u = -1$. So $d\theta' \sin\theta' = -du$. The limits change from $0 \to \pi$ to $1 \to -1$, which reverses the sign, so we can write it as $\int_{-1}^{1} du$.

$$I_z(\lambda \to \infty) = 2\pi\rho_E \int_0^{R_E} dr' r'^2 \int_{-1}^{1} du \frac{D - r'u}{\left(r'^2 + D^2 - 2Dr'u\right)^{3/2}} \tag{80}$$

This inner integral is of the form $\int \frac{A+Bu}{(C+Du)^{3/2}} du$. Let's substitute u in terms of r.

From $r^2 = r'^2 + D^2 - 2Dr'u$, we get $2Dr'u = r'^2 + D^2 - r^2$. So,

$$u = \frac{r'^2 + D^2 - r^2}{2Dr'} \tag{81}$$

Also, $2rdr = -2Dr'du \Rightarrow du = -\frac{rdr}{Dr'}$. The limits for u are $u = -1 \Rightarrow r = D + r'$ and $u = 1 \Rightarrow r = |D - r'| = D - r'$ (since $D > R_E \geq r'$). And

$$\frac{D - r'u}{r} = \frac{D^2 - r'^2 + r^2}{2Dr} \tag{82}$$

Substituting these into the inner integral (let's call it $K(r')$ again):

$$\begin{aligned} K(r') &= \int_{D-r'}^{D+r'} \left(\frac{rdr}{Dr'}\right) \frac{D^2 - r'^2 + r^2}{2Dr} \frac{1}{r^2} \\ &= \frac{1}{2D^2 r'} \int_{D-r'}^{D+r'} \left(\frac{D^2 - r'^2}{r^2} + 1\right) dr \end{aligned} \tag{83}$$

Performing the integral respect r:

$$K(r') = \frac{1}{2D^2 r'} \left[\left(D^2 - r'^2\right)\left(-\frac{1}{r}\right) + r\right]_{D-r'}^{D+r'} \tag{84}$$

This is,

$$K(r') = \frac{2}{D^2} \tag{85}$$

Finally,

$$\begin{aligned} I_z(\lambda \to \infty) &= 2\pi\rho_E \int_0^{R_E} dr' r'^2 K(r') = 2\pi\rho_E \int_0^{R_E} dr' r'^2 \left(\frac{2}{D^2}\right) \\ &= \frac{4\pi\rho_E}{D^2} \int_0^{R_E} r'^2 dr' = \frac{4\pi\rho_E}{D^2} \left[\frac{r'^3}{3}\right]_0^{R_E} = \frac{4\pi\rho_E}{D^2} \frac{R_E^3}{3} \end{aligned} \tag{86}$$

Since $M_{\text{nucl\_E}} = \frac{4}{3}\pi R_E^3 \rho_E$

$$I_z(\lambda \to \infty) = \frac{M_{nucl_2 E}}{D_E^2} \tag{87}$$

C. Tungsten

We make the following assumptions for the Tungsten source:

1. The radius of the cylinder is $R = 0.01\mathrm{m}$.
2. The height of the cylinder is $H = 0.01\mathrm{m}$.
3. The density of tungsten is $\rho_W = 19.25 \times 10^3\ \mathrm{kg/m}^3$.
4. The cylinder's center is placed at the origin of the coordinate system. Therefore, the range for the vertical coordinate z' of a source element is $z' \in [-H/2, H/2]$.
5. The detector is placed along the z-axis at a position vector $r_{\text{det}} = (0, 0, H/2 + d)$. We define $D_{\text{top}} = H/2 + d$ as the z-coordinate of the detector.
6. The distance d from the detector to the center of the top face of the Tungsten cylinder is $d = 100\mu\mathrm{m} = 10^{-4}\,\mathrm{m}$.

Starting from Eq. (29), which defines the integral for the pseudo-magnetic field due to a generic source, we adapt it for the Tungsten cylinder geometry:

$$I_z(\lambda) = \int_{\text{source}} dV' \rho\left(r'\right) \frac{D_{\text{top}} - z'}{r} \left(\frac{1}{r\lambda} + \frac{1}{r^2}\right) e^{-r/\lambda} \tag{88}$$

Here, we clarify the variables:

- r': The position vector of a differential volume element within the Tungsten source.
- r_{det}: The position vector of the detector.
- r: The magnitude of the vector from the source element to the detector, defined as $r = |r_{\text{det}} - r'|$. In cylindrical coordinates, with the detector at $(0, 0, D_{\text{top}})$ and a source element at $(\rho' \cos\phi', \rho' \sin\phi', z')$, this distance is calculated as:

$$r = \sqrt{(\rho' \cos\phi' - 0)^2 + (\rho' \sin\phi' - 0)^2 + (z' - D_{\text{top}})^2} = \sqrt{\rho'^2 + (D_{\text{top}} - z')^2}$$

- $\rho\left(r'\right)$: The nucleon density of the source, which is ρ_W for the Tungsten cylinder.

The volume element in cylindrical coordinates is $dV' = \rho' d\rho' d\phi' dz'$. Due to the azimuthal symmetry of the cylinder and the detector's position along the z-axis, the integral over ϕ' will yield 2π. Thus, the integral for I_z^{cylinder} becomes:

$$\begin{aligned} I_z^{\text{cylinder}}\left(\lambda, R, H, d, \rho_p\right) &= \rho_p \int_{z'=-H/2}^{H/2} dz' \int_{\rho'=0}^{R} d\rho' \rho' \int_{\phi'=0}^{2\pi} d\phi' \frac{D_{\text{top}} - z'}{r} \left(\frac{1}{r\lambda} + \frac{1}{r^2}\right) e^{-r/\lambda} \\ &= 2\pi \rho_p \int_{-H/2}^{H/2} dz' \int_0^R d\rho' \rho' \frac{D_{\text{top}} - z'}{r} \left(\frac{1}{r\lambda} + \frac{1}{r^2}\right) e^{-r/\lambda} \end{aligned} \tag{89}$$

D Derivation of the Non-Relativistic Limit of the Curved-Spacetime Dirac Hamiltonian

The purpose of this appendix is to show the derivation of the non-relativistic Hamiltonian for a spin-1/2 fermion interacting with both electromagnetic and weak gravitational fields. This derivation is essential because standard quantum mechanics is formulated in flat spacetime, whereas a gravitational wave is, by definition, a dynamic curvature of spacetime. To accurately model how a quantum sensor responds to such a wave, we must begin with the fully covariant Dirac equation in curved spacetime and then systematically find its non-relativistic limit, which is the physical regime of a laboratory experiment.

The method we employ is the Foldy-Wouthuysen (FW) transformation. This is a standard technique in theoretical physics used to decouple the positive-energy (particle) and negative-energy (antiparticle) solutions of the Dirac equation. By applying a series of unitary transformations, we can systematically eliminate terms that mix these components, obtaining a block-diagonal Hamiltonian whose upper block corresponds to the physically meaningful non-relativistic Hamiltonian for a particle.

D.1 Conventions

To ensure clarity and reproducibility, we adopt the following conventions throughout this derivation:

1. Metric: We use the mostly-plus metric signature, $\eta_{ab} = \mathrm{diag}(-1, 1, 1, 1)$.
2. Dirac Matrices: We use the Bjorken & Drell convention [28] for the gamma matrices (γ^μ).
3. Indices: Greek indices ($\mu, \nu, \dots$) denote spacetime coordinates in the general curved spacetime frame, while Latin indices ($a, b, \dots$) denote coordinates in the local, flat Minkowski frame of an observer.
4. Tetrads: The tetrad field, e_u^a, is used to relate the two frames.

D.2 Hamiltonian

Our derivation begins with the fully covariant Dirac equation for a fermion of mass m and charge e in a curved spacetime with metric $g_{\mu\nu}$, coupled to an electromagnetic four-potential A_μ :

$$\left[\hbar c\gamma^\mu\left(\partial_\mu + \Gamma_\mu + \frac{ie}{\hbar c}A_\mu\right) + mc^2\right]\psi = 0, \tag{90}$$

Here, ψ is the four-component Dirac spinor, $\gamma^\mu = e^\mu_a\hat{\gamma}^a$ are the curved-space gamma matrices (where $\hat{\gamma}^a$ are the standard flat-space matrices), and Γ_μ is the spin connection, which encodes the interaction between the fermion's spin and the spacetime curvature.

The first step is to derive the corresponding Hamiltonian, H, that governs the time evolution of the spinor, ψ, such that $i\hbar\partial_t\psi = H\psi$. This is achieved by separating the time and space components of the covariant Dirac equation, leading to [5]

$$H = -i\left[\hbar c g_{00}\gamma^0\gamma^i\left(\partial_i + \Gamma_i + \frac{ie}{\hbar c}A_i\right) + \hbar c\Gamma_0 - ie\phi + g_{00}\gamma^0 mc^2\right]. \tag{92}$$

---

[5] Notice that by taking the flat-space limit, where $g_{00}\gamma^0 \to \alpha^i$ and $g_{00}\gamma^0 \to i\beta$, we recover:

$$i\hbar\partial_t\psi = (-i\hbar c\nabla + eA)\cdot\alpha\psi + \beta mc^2\psi - e\phi\psi, \tag{91}$$

which corresponds to the standard Dirac equation in flat space.

The resulting Hamiltonian, however, is still expressed in terms of curved-space gamma matrices (γ^μ) and the general spin connection (Γ_μ). To make it ready for the FW transformation, which operates on standard Dirac matrices, we must transform the Hamiltonian into the local inertial frame (LIF) of the detector. This is done using the tetrad formalism.

We expand the metric in the weak-field limit, $g_{\mu\nu} = \eta_{\mu\nu} + h_{\mu\nu}$, and use the corresponding tetrads

$$\begin{aligned} e_a{}^\mu &= \begin{pmatrix} 1+\frac{1}{2}h_{00} & -\frac{1}{2}h_{0i} \\ \frac{1}{2}h_{0i} & \delta_{ij}-\frac{1}{2}h_{ij} \end{pmatrix}, \\ e^a{}_\mu &= \begin{pmatrix} 1-\frac{1}{2}h_{00} & -\frac{1}{2}h_{0i} \\ \frac{1}{2}h_{0i} & \delta_{ij}+\frac{1}{2}h_{ij} \end{pmatrix}, \end{aligned} \tag{93}$$

to express all curved-space quantities in terms of the flat-space Dirac matrices ($\hat{\gamma}^a$) and the gravitational perturbation ($h_{\mu\nu}$). This process, which involves substituting the expressions for the tetrads and the spin connection

$$\Gamma_\mu \simeq \frac{1}{2}\sigma^{ab}\left(\frac{1}{2}\partial_\mu h_{ba} - \Gamma^\lambda_{\mu a}\eta_{b\lambda}\right). \tag{94}$$

into the general Hamiltonian, Eq. 92, is algebraically intensive. After significant simplification, which includes applying standard gamma matrix identities

$$\begin{aligned} \alpha^i\alpha^j\alpha^k &= \eta^{ij}\alpha^k + \eta^{jk}\alpha^i - \eta^{ik}\alpha^j + i\epsilon^{0ijk}\hat{\gamma}^5, \\ \Rightarrow \alpha^i\alpha^j\alpha^k\left(\partial_k h_{ij} - \partial_j h_{ik}\right) &= 2\alpha^i\left(\partial_i h_{jj} - \partial_j h_{ij}\right), \end{aligned} \tag{95}$$

we arrive at the final Hamiltonian for the coupled gravitational-electromagnetic-spinor system, expressed entirely in the local frame

$$\begin{aligned} \mathcal{H} = &\left(1-\frac{1}{2}h_{00}\right)\alpha^i\Pi_i - \frac{1}{2}h_{0j}\alpha^j\alpha^i\Pi_i - \frac{1}{2}\left[h_{0i} + h_{ij}\alpha^j\right]\Pi_i\mathbb{I}_4 \\ &- \frac{i\hbar c}{4}\left[-\partial_i h_{0i}\mathbb{I}_4 - \alpha^i\left(\partial_i h_{00} - \partial_i h_{jj} + \partial_j h_{ij} - \frac{1}{c}\partial_t h_{0i}\right) + \alpha^i\alpha^j\partial_0 h_{ij}\right] \\ &+ eA_0\mathbb{I}_4 + \left(1-\frac{1}{2}h_{00}\right)\beta mc^2 - \frac{1}{2}\left(h_{0i}\alpha^i\right)\beta mc^2. \end{aligned} \tag{96}$$

where we have defined, for brevity:

$$\Pi_i = \left(-i\hbar c\vec{\nabla} + e\vec{A}\right). \tag{97}$$

D.3 The Foldy-Wouthuysen Transformation

The Hamiltonian derived from the Dirac equation contains operators that mix the particle and antiparticle components of the spinor ψ. These are known as "odd" operators (block off-diagonal in the Dirac representation), which we seek to eliminate. The FW procedure consists of applying a series of unitary transformations, $H' = e^{iS}He^{-iS} - i\hbar e^{iS}\left(\partial_t e^{-iS}\right)$, where the Hermitian operator S is chosen at each step to cancel the leading odd term, $\mathcal{O}$, according to the relation $S = -i\frac{\beta\mathcal{O}}{2mc^2}$. We apply this procedure iteratively to eliminate all odd terms up to the desired order in $1/m$.

Let's begin with the Hamiltonian

$$\begin{aligned}\mathcal{H} =& \left(1-\frac{1}{2}\overset{\mathcal{E}}{h_{00}}\right)\alpha^i\Pi_i - \frac{1}{2}h_{0j}\overset{\mathcal{E}}{\alpha^j}\alpha^i\Pi_i - \frac{1}{2}\left[\overset{\mathcal{E}}{h_{0i}} + \overset{\mathcal{O}}{h_{ij}}\alpha^j\right]\Pi_i\mathbb{1}_4 \\ &- \frac{i\hbar c}{4}\left[-\partial_i\overset{\mathcal{E}}{h_{0i}}\mathbb{1}_4 - \alpha^i\left(\partial_i h_{00} - \overset{\mathcal{O}}{\partial_i h_{jj}} + \partial_j h_{ij} - \frac{1}{c}\partial_t h_{0i}\right) + \alpha^i\overset{\mathcal{E}}{\alpha^j}\partial_0 h_{ij}\right] \\ &+ e\overset{\mathcal{E}}{A_0}\mathbb{1}_4 + \left(1-\frac{1}{2}\overset{\mathcal{E}}{h_{00}}\right)\beta mc^2 - \frac{1}{2}\left(h_{0i}\overset{\mathcal{O}}{\alpha^i}\right)\beta mc^2.\end{aligned} \tag{98}$$

S1

$$S_1 = -\frac{i}{4}h_{0i}\alpha^i \tag{99}$$

$$iL_{S_1}\left[\alpha^j\left(-i\hbar c\partial_j + eA_j\right)\right] = \frac{1}{2}h_{0i}\mathbb{1}_4\Pi_i - \frac{1}{2}h_{0j}\alpha^i\alpha^j(-i\hbar c\partial_i + eA_i) + \frac{i\hbar c}{4}\alpha^j\alpha^i\partial_j h_{0i} \tag{100}$$

$$iL_s\left[\beta mc^2\right] = \frac{1}{2}h_{0i}\alpha^i\beta mc^2 \tag{101}$$

$$-\hbar\dot{S}_1 = \frac{i\hbar c}{4}\alpha^i\frac{1}{c}\partial_t h_{0i} \tag{102}$$

After applying the unitary transformation S_1, the resulting transformed Hamiltonian, denoted as $\mathcal{H}'$, is expressed as follows:

$$\begin{aligned}\mathcal{H}' =& \left(1-\frac{1}{2}\overset{\mathcal{O}}{h_{00}}\right)\alpha^i\Pi_i - \overset{\mathcal{E}}{h_{0i}}\mathbb{1}_4\Pi_i - \frac{1}{2}\overset{\mathcal{O}}{\alpha^j}h_{ij}\Pi_i \\ &+ \frac{i\hbar c}{4}\left[\partial_i\overset{\mathcal{E}}{h_{0i}}\mathbb{1}_4 + \alpha^i\left(\partial_i h_{00} - \overset{\mathcal{O}}{\partial_i h_{jj}} + \partial_j h_{ij}\right) - \alpha^i\alpha^j\left(\partial_0\overset{\mathcal{E}}{h_{ij}} - \partial_i h_{0j}\right)\right] \\ &+ e\overset{\mathcal{E}}{A_0}\mathbb{1}_4 + \left(1-\frac{1}{2}\overset{\mathcal{E}}{h_{00}}\right)\beta mc^2\end{aligned} \tag{103}$$

S2

$$S_2 = \frac{\hbar}{8mc}\beta\alpha^i(\partial_i h_{00} - \partial_i h_{jj} + \partial_j h_{ij}) \tag{104}$$

with $D_{ij} := (\partial_i h_{00} - \partial_i h_{jj} + \partial_j h_{ij})$

$$iL_{S_2}\left[\alpha^k\left(-i\hbar c\partial_k + eA_k\right)\right] = \frac{i\hbar}{4mc}\beta D_{ij}\Pi_i + \frac{\hbar^2}{8m}\beta\alpha^k\alpha^i\partial_k D_{ij} \tag{105}$$

$$iL_{S_2}\left[\beta mc^2\right] = -\frac{i\hbar c}{4}\alpha^i\left(\partial_i h_{00} - \partial_i h_{jj} + \partial_j h_{ij}\right) \tag{106}$$

$$-\hbar\dot{S}_2 = -\frac{\hbar^2}{8mc}\beta\alpha^i\left(\partial_t\partial_i h_{00} - \partial_t\partial_i h_{jj} + \partial_t\partial_j h_{ij}\right) \tag{107}$$

After applying the unitary transformation S_2, the resulting transformed Hamiltonian, denoted as $\mathcal{H}''$, is expressed as follows:

$$\begin{aligned}\mathcal{H}'' =& \left(1-\frac{1}{2}\overset{\mathcal{O}}{h_{00}}\right)\alpha^i\Pi_i - \frac{1}{2}\overset{\mathcal{O}}{\alpha^j}h_{ij}\Pi_i - \overset{\mathcal{E}}{h_{0i}}\mathbb{1}_4\Pi_i + \frac{i\hbar c}{4}\left[3\partial_i\overset{\mathcal{E}}{h_{0i}}\mathbb{1}_4 - \partial_0\overset{\mathcal{E}}{h_{ii}}\mathbb{1}_4 - \alpha^i\overset{\mathcal{E}}{\alpha^j}\partial_j h_{0i}\right] \\ &+ \frac{i\hbar}{4mc}\overset{\mathcal{E}}{\beta}D_{ij}\Pi_i + \frac{\hbar^2}{8m}\left(\beta\alpha^k\overset{\mathcal{E}}{\alpha^i}\partial_k D_{ij} - \beta\alpha^i\overset{\mathcal{O}}{\partial_0}D_{ij}\right) + e\overset{\mathcal{E}}{A_0}\mathbb{1}_4 + \left(1-\frac{1}{2}\overset{\mathcal{E}}{h_{00}}\right)\beta mc^2\end{aligned} \tag{108}$$

S3

$$S_3 = -\frac{i}{2mc^2}\beta\alpha^i\Pi_i \tag{109}$$

$$iL_{S_3}\left[\left(1-\frac{1}{2}h_{00}\right)\alpha^j\Pi_j\right] = \frac{1}{mc^2}\beta\alpha^i\alpha^j\left(1-\frac{1}{2}h_{00}\right)\Pi_i\Pi_j + \frac{i\hbar}{4mc}\beta\alpha^i\alpha^j\partial_i(h_{00})\Pi_j \tag{110}$$

$$iL_{S_3}\left[-\mathbb{I}_4 h_{0j}\left(-i\hbar c\partial_j + eA_j\right)\right] = \frac{1}{2mc^2}\beta\alpha^i h_{0j}\left[\Pi_i,\Pi_j\right] - \frac{i\hbar}{2mc}\beta\alpha^i\partial_i h_{0j}\Pi_j. \tag{111}$$

$$iL_{S_3}\left[-\frac{1}{2}h_{jk}\alpha^k\left(-i\hbar c\partial_j + eA_j\right)\right] = \frac{i\hbar}{4mc}\beta\alpha^i\alpha^k\partial_i h_{jk}\Pi_j - \frac{1}{4mc^2}\beta\alpha^i\alpha^k h_{jk}[\Pi_i,\Pi_j] - \frac{1}{2mc^2}\beta h_{ij}\Pi_j\Pi_i \tag{112}$$

$$iL_{S_3}\left[-\frac{i\hbar c}{4}\alpha^j\alpha^k\partial_k h_{0j}\right] = -\frac{i\hbar}{4mc}\beta\alpha^i\left(\partial_i h_{0j} - \partial_j h_{0i}\right)\Pi_j - \frac{\hbar^2}{4m}\beta\alpha^i\partial_i\partial_j h_{0j} + \frac{\hbar^2}{8m}\beta\alpha^i\partial_j\partial_j h_{0i} \tag{113}$$

$$iL_{S_3}\left[eA_0\mathbb{I}_4\right] = \frac{-i\hbar e}{2mc}\beta\alpha^i\partial_i A_0 \tag{114}$$

$$iL_{S_3}\left[\left(1-\frac{1}{2}h_{00}\right)\beta mc^2\right] = -\left(1-\frac{1}{2}h_{00}\right)\alpha^i\Pi_i - \frac{i\hbar c}{4}\alpha^i\partial_i h_{00} \tag{115}$$

$$-\hbar\dot{S}_3 = \frac{i\hbar e}{2mc}\beta\alpha^i\partial_0 A_i \tag{116}$$

$$\begin{aligned}-\frac{1}{2}L_{S_3}^2\left[\left(1-\frac{1}{2}h_{00}\right)\beta mc^2\right] = &-\frac{1}{2mc^2}\beta\alpha^i\alpha^j\left(1-\frac{1}{2}h_{00}\right)\Pi_i\Pi_j + \frac{i\hbar}{8mc}\beta\alpha^i\alpha^j\partial_i h_{00}\Pi_j|_{i\neq j}\\ &-\frac{\hbar^2}{16m}\beta\partial_i\partial_i h_{00}\end{aligned} \tag{117}$$

After applying the unitary transformation S_3, the resulting transformed Hamiltonian, denoted as $\mathcal{H}'''$, is expressed as follows:

$$\begin{aligned}\mathcal{H}''' = &-\frac{1}{2}\alpha^j h_{ij}\Pi_i - h_{0i}\Pi_i\mathbb{I}_4 + \frac{1}{2mc^2}\beta\alpha^i\alpha^j\left(1-\frac{1}{2}h_{00}\right)\Pi_i\Pi_j\\ &+\frac{i\hbar c}{4}\left[3\partial_i h_{0i}\mathbb{I}_4 - \partial_0 h_{ii}\mathbb{I}_4 - \alpha^i\alpha^j\partial_j h_{0i} - \alpha^i\partial_i h_{00}\right] + \frac{i\hbar}{4mc}\beta D_{ij}\Pi_i + \frac{\hbar^2}{8m}\left(\beta\alpha^k\alpha^i\partial_k D_{ij} - \beta\alpha^i\partial_0 D_{ij}\right)\\ &+\frac{i\hbar}{4mc}\left[\beta\alpha^i\alpha^j\partial_i h_{00} - 2\beta\alpha^i\partial_i h_{0j} + \beta\alpha^i\alpha^k\partial_i h_{jk} - \beta\alpha^i\left(\partial_i h_{0j} - \partial_j h_{0i}\right) + \frac{1}{2}\beta\alpha^i\alpha^j\partial_i h_{00}\Big|_{i\neq j}\right]\Pi_j\\ &+\frac{1}{2mc^2}\left[\left(\beta\alpha^i h_{0j} - \frac{1}{2}\beta\alpha^i\alpha^k h_{jk}\right)[\Pi_i,\Pi_j] - \beta h_{ij}\Pi_j\Pi_i\right] + \frac{\hbar^2}{8m}\beta\left[\alpha^i\left(-2\partial_i\partial_j h_{0j} + \partial_j\partial_j h_{0i}\right) - \frac{1}{2}\partial_i\partial_i h_{00}\right]\\ &-\frac{i\hbar e}{2mc}\beta\alpha^i\left(\partial_i A_0 - \partial_0 A_i\right) + eA_0\mathbb{I}_4 + \left(1-\frac{1}{2}h_{00}\right)\beta mc^2\end{aligned} \tag{118}$$

S4

$$S_4 = \frac{i}{4mc^2}\beta\alpha^j h_{ij}\Pi_i \tag{119}$$

$$
\begin{aligned}
iL_{s_4}\left[eA_0\mathbb{I}_4\right] &= \frac{i\hbar e}{4mc}\beta\alpha^j h_{ij}\partial_i A_0 \\
iL_{s_4}\left[\beta mc^2\right] &= \frac{1}{2}\alpha^j h_{ij}\Pi_i \\
-\hbar\dot{S}_4 &= -\frac{i\hbar e}{4mc}\beta\alpha^j h_{ij}\partial_0 A_i
\end{aligned}
\tag{120}
$$

After applying the unitary transformation S_4, the resulting transformed Hamiltonian, denoted as $\mathcal{H}^{IV}$, is expressed as follows:

$$
\begin{aligned}
\mathcal{H}^{IV} &= -h_{0i}\Pi_i\mathbb{I}_4 + \frac{1}{2mc^2}\beta\alpha^i\alpha^j\left(1-\frac{1}{2}h_{00}\right)\Pi_i\Pi_j \\
&+ \frac{i\hbar c}{4}\left[3\partial_i h_{0i}\mathbb{I}_4 - \partial_0 h_{ii}\mathbb{I}_4 - \alpha^i\alpha^j\partial_j h_{0i} - \alpha^i\partial_i h_{00}\right] + \frac{i\hbar}{4mc}\beta D_{ij}\Pi_i + \frac{\hbar^2}{8m}\left(\beta\alpha^k\alpha^i\partial_k D_{ij} - \beta\alpha^i\partial_0 D_{ij}\right) \\
&+ \frac{i\hbar}{4mc}\left[\beta\alpha^i\alpha^j\partial_i h_{00} - 2\beta\alpha^i\partial_i h_{0j} + \beta\alpha^i\alpha^k\partial_i h_{jk} - \beta\alpha^i\left(\partial_i h_{0j} - \partial_j h_{0i}\right) + \frac{1}{2}\beta\alpha^i\alpha^j\partial_i h_{00}\Big|_{i\neq j}\right]\Pi_j \\
&+ \frac{1}{2mc^2}\left[\left(\beta\alpha^i h_{0j} - \frac{1}{2}\beta\alpha^i\alpha^k h_{jk}\right)\left[\Pi_i,\Pi_j\right] - \beta h_{ij}\Pi_j\Pi_i\right] + \frac{h^2}{8m}\beta\left[\alpha^i\left(-2\partial_i\partial_j h_{0j} + \partial_j\partial_j h_{0i}\right) - \frac{1}{2}\partial_i\partial_i h_{00}\right] \\
&- \frac{i\hbar e}{2mc}\left[\beta\alpha^i\left(\partial_i A_0 - \partial_0 A_i\right) - \frac{1}{2}\beta\alpha^j h_{ij}\left(\partial_i A_0 - \partial_0 A_i\right)\right] + eA_0\mathbb{I}_4 + \left(1-\frac{1}{2}h_{00}\right)\beta mc^2
\end{aligned}
\tag{121}
$$

S5

$$
S_5 = -\frac{\hbar}{8mc}\beta\alpha^i\partial_i h_{00}
\tag{122}
$$

$$
iL_{S5}\left[\beta mc^2\right] = \frac{i\hbar c}{4}\alpha^i\partial_i h_{00}
\tag{123}
$$

$$
-\hbar\dot{S}_5 = \frac{\hbar^2}{8m}\beta\alpha^i\partial_0\partial_i h_{00}
\tag{124}
$$

After applying the unitary transformation S_5, the resulting transformed Hamiltonian, denoted as $\mathcal{H}^{V}$, is expressed as follows:

$$
\begin{aligned}
H^{V} &= -h_{0i}\Pi_i\mathbb{I}_4 + \frac{1}{2mc^2}\beta\alpha^i\alpha^j\left(1-\frac{1}{2}h_{00}\right)\Pi_i\Pi_j + \frac{i\hbar c}{4}\left[3\partial_i h_{0i}\mathbb{I}_4 - \partial_0 h_{ii}\mathbb{I}_4 - \alpha^i\alpha^j\partial_j h_{0i}\right] \\
&+ \frac{i\hbar}{4mc}\beta D_{ij}\Pi_i + \frac{\hbar^2}{8m}\left(\beta\alpha^k\alpha^i\partial_k D_{ij}\right) - \frac{\hbar^2}{8m}\beta\alpha^i\partial_0\left(\partial_j h_{ij} - \partial_i h_{jj}\right) \\
&+ \frac{i\hbar}{4mc}\left[\beta\alpha^i\alpha^j\partial_i h_{00} - 2\beta\alpha^i\partial_i h_{0j} + \beta\alpha^i\alpha^k\partial_i h_{jk} - \beta\alpha^i\left(\partial_i h_{0j} - \partial_j h_{0i}\right) + \frac{1}{2}\beta\alpha^i\alpha^j\partial_i h_{00}\Big|_{i\neq j}\right]\Pi_j \\
&+ \frac{1}{2mc^2}\left[\left(\beta\alpha^i h_{0j} - \frac{1}{2}\beta\alpha^i\alpha^k h_{jk}\right)\left[\Pi_i,\Pi_j\right] - \beta h_{ij}\Pi_j\Pi_i\right] + \frac{\hbar^2}{8m}\beta\left[\alpha^i\left(-2\partial_i\partial_j h_{0j} + \partial_j\partial_j h_{0i}\right) - \frac{1}{2}\partial_i\partial_i h_{00}\right] \\
&- \frac{i\hbar e}{2mc}\left[\beta\alpha^i\left(\partial_i A_0 - \partial_0 A_i\right) - \frac{1}{2}\beta\alpha^j h_{ij}\left(\partial_i A_0 - \partial_0 A_i\right)\right] + eA_0\mathbb{I}_4 + \left(1-\frac{1}{2}h_{00}\right)\beta mc^2
\end{aligned}
\tag{125}
$$

S6

$$
S_6 = \frac{i\hbar^2}{16m^2c^2}\alpha^i\partial_0\left(\partial_j h_{ij} - \partial_i h_{ij}\right)
\tag{126}
$$

$$
iL_{S6}\left[\beta mc^2\right] = \frac{\hbar^2}{8m}\beta\alpha^i\partial_0\left(\partial_j h_{ij} - \partial_i h_{jj}\right)
\tag{127}
$$

After applying the unitary transformation S_6, the resulting transformed Hamiltonian, denoted as $\mathcal{H}^{VI}$, is expressed as follows:

$$\begin{aligned}\mathcal{H}^{VI} &= -h_{0i}\Pi_i\mathbb{1}_4 + \frac{1}{2mc^2}\beta\alpha^i\alpha^j\left(1-\frac{1}{2}h_{00}\right)\Pi_i\Pi_j + \frac{i\hbar c}{4}\left[3\partial_i h_{0i}\mathbb{1}_4 - \partial_0 h_{ii}\mathbb{1}_4 - \alpha^i\alpha^j\partial_j h_{0i}\right]\\ &+ \frac{i\hbar}{4mc}\beta D_{ij}\Pi_i + \frac{\hbar^2}{8m}\beta\alpha^k\alpha^i\partial_k D_{ij}\\ &+ \frac{i\hbar}{4mc}\left[\beta\alpha^i\alpha^j\partial_i h_{00} - 2\beta\alpha^i\partial_i h_{0j} + \beta\alpha^i\alpha^k\partial_i h_{jk} - \beta\alpha^i\left(\partial_i h_{0j} - \partial_j h_{0i}\right) + \frac{1}{2}\beta\alpha^i\alpha^j\partial_i h_{00}\Big|_{i\neq j}\right]\Pi_j\\ &+ \frac{1}{2mc^2}\left[\left(\beta\alpha^i h_{0j} - \frac{1}{2}\beta\alpha^i\alpha^k h_{jk}\right)[\Pi_i,\Pi_j] - \beta h_{ij}\Pi_j\Pi_i\right] + \frac{\hbar^2}{8m}\beta\left[\alpha^i\left(-2\partial_i\partial_j h_{0j} + \partial_j\partial_j h_{0i}\right) - \frac{1}{2}\partial_i\partial_i h_{00}\right]\\ &- \frac{i\hbar e}{2mc}\left[\beta\alpha^i\left(\partial_i A_0 - \partial_0 A_i\right) - \frac{1}{2}\beta\alpha^j h_{ij}\left(\partial_i A_0 - \partial_0 A_i\right)\right] + eA_0\mathbb{1}_4 + \left(1-\frac{1}{2}h_{00}\right)\beta mc^2\end{aligned} \tag{128}$$

S7

$$S_7 = -\frac{\hbar}{4m^2c^3}\alpha^i\partial_i h_{0j}\Pi_j \tag{129}$$

$$iL_{S7}\left[\beta mc^2\right] = +\frac{i\hbar}{2mc}\beta\alpha^i\partial_i h_{0j}\Pi_j \tag{130}$$

After applying the unitary transformation S_7, the resulting transformed Hamiltonian, denoted as H^{VII} is expressed as follows:

$$\begin{aligned}H^{VII} &= -h_{0i}\Pi_i\mathbb{1}_4 + \frac{1}{2mc^2}\beta\alpha^i\alpha^j\left(1-\frac{1}{2}h_{00}\right)\Pi_i\Pi_j + \frac{i\hbar c}{4}\left[3\partial_i h_{0i}\mathbb{1}_4 - \partial_0 h_{ii}\mathbb{1}_4 - \alpha^i\alpha^j\partial_j h_{0i}\right]\\ &+ \frac{i\hbar}{4mc}\beta D_{ij}\Pi_i + \frac{\hbar^2}{8m}\beta\alpha^k\alpha^i\partial_k D_{ij}\\ &+ \frac{i\hbar}{4mc}\left[\beta\alpha^i\alpha^j\partial_i h_{00} + \beta\alpha^i\alpha^k\partial_i h_{jk} - \beta\alpha^i\left(\partial_i h_{0j} - \partial_j h_{0i}\right) + \frac{1}{2}\beta\alpha^i\alpha^j\partial_i h_{00}\Big|_{i\neq j}\right]\Pi_j\\ &+ \frac{1}{2mc^2}\left[\left(\beta\alpha^i h_{0j} - \frac{1}{2}\beta\alpha^i\alpha^k h_{jk}\right)[\Pi_i,\Pi_j] - \beta h_{ij}\Pi_j\Pi_i\right]\Bigg] + \frac{\hbar^2}{8m}\beta\left[\alpha^i\left(-2\partial_i\partial_j h_{0j} + \partial_j\partial_j h_{0i}\right) - \frac{1}{2}\partial_i\partial_i h_{00}\right]\\ &- \frac{i\hbar e}{2mc}\left[\beta\alpha^i\left(\partial_i A_0 - \partial_0 A_i\right) - \frac{1}{2}\beta\alpha^j h_{ij}\left(\partial_i A_0 - \partial_0 A_i\right)\right] + eA_0\mathbb{1}_4 + \left(1-\frac{1}{2}h_{00}\right)\beta mc^2\end{aligned} \tag{131}$$

S8

$$S_8 = -\frac{\hbar}{8m^2c^3}\alpha^i\left(\partial_i h_{0j} - \partial_j h_{0i}\right)\Pi_j \tag{132}$$

$$iL_{S8}\left[\beta mc^2\right] = \frac{i\hbar}{4mc}\beta\alpha^i\left(\partial_i h_{0j} - \partial_j h_{0i}\right)\Pi_j \tag{133}$$

After applying the unitary transformation S_8, the resulting transformed Hamiltonian, denoted as H^{VIII} is expressed as follows:

$$\begin{aligned}H^{VIII} &= -h_{0i}\Pi_i\mathbb{1}_4 + \frac{1}{2mc^2}\beta\alpha^i\alpha^j\left(1-\frac{1}{2}h_{00}\right)\Pi_i\Pi_j + \frac{i\hbar c}{4}\left[3\partial_i h_{0i}\mathbb{1}_4 - \partial_0 h_{ii}\mathbb{1}_4 - \alpha^i\alpha^j\partial_j h_{0i}\right]\\ &+ \frac{i\hbar}{4mc}\beta D_{ij}\Pi_i + \frac{\hbar^2}{8m}\beta\alpha^k\alpha^i\partial_k D_{ij} + \frac{i\hbar}{4mc}\left[\beta\alpha^i\alpha^j\partial_i h_{00+}\beta\alpha^i\alpha^k\partial_i h_{jk} + \frac{1}{2}\beta\alpha^i\alpha^j\partial_i h_{00}\Big|_{i\neq j}\right]\Pi_j\\ &+ \frac{1}{2mc^2}\left[\left(\beta\alpha^i h_{0j} - \frac{1}{2}\beta\alpha^i\alpha^k h_{jk}\right)[\Pi_i,\Pi_j] - \beta h_{ij}\Pi_j\Pi_i\right] + \frac{\hbar^2}{8m}\beta\left[\alpha^i\left(-2\partial_i\partial_j h_{0j} + \partial_j\partial_j h_{0i}\right) - \frac{1}{2}\partial_i\partial_i h_{00}\right]\\ &- \frac{i\hbar e}{2mc}\left[\beta\alpha^i\left(\partial_i A_0 - \partial_0 A_i\right) - \frac{1}{2}\beta\alpha^j h_{ij}\left(\partial_i A_0 - \partial_0 A_i\right)\right] + eA_0\mathbb{1}_4 + \left(1-\frac{1}{2}h_{00}\right)\beta mc^2\end{aligned} \tag{134}$$

S9

$$S_q = \frac{-i}{4m^2c^4}\alpha^i h_{0j}\left[\Pi_i, \Pi_j\right] \tag{135}$$

$$il_{S9}\left[\beta mc^2\right] = -\frac{1}{2mc^2}\beta\alpha^i h_{0j}\left[\Pi_i, \Pi_j\right] \tag{136}$$

After applying the unitary transformation S_9, the resulting transformed Hamiltonian, denoted as H^{IX} is expressed as follows:

$$\begin{aligned}
\mathcal{H}^{IX} &= -h_{0i}\Pi_i\mathbb{1}_4 + \frac{1}{2mc^2}\beta\alpha^i\alpha^j\left(1-\frac{1}{2}h_{00}\right)\Pi_i\Pi_j + \frac{i\hbar c}{4}\left[3\partial_i h_{0i}\mathbb{1}_4 - \partial_0 h_{ii}\mathbb{1}_4 - \alpha^i\alpha^j\partial_j h_{0i}\right] \\
&+ \frac{i\hbar}{4mc}\beta D_{ij}\Pi_i + \frac{\hbar^2}{8m}\beta\alpha^k\alpha^i\partial_k D_{ij} + \frac{i\hbar}{4mc}\left[\beta\alpha^i\alpha^j\partial_i h_{00} + \beta\alpha^i\alpha^k\partial_i h_{jk} + \frac{1}{2}\beta\alpha^i\alpha^j\partial_i h_{00}\Big|_{i\neq j}\right]\Pi_j \\
&+ \frac{1}{2mc^2}\left[-\frac{1}{2}\beta\alpha^i\alpha^k h_{jk}\left[\Pi_i, \Pi_j\right] - \beta h_{ij}\Pi_j\Pi_i\right] + \frac{\hbar^2}{8m}\beta\left[\alpha^i\left(-2\partial_i\partial_j h_{0j} + \partial_j\partial_j h_{0i}\right) - \frac{1}{2}\partial_i\partial_i h_{00}\right] \\
&- \frac{i\hbar e}{2mc}\left[\beta\alpha^i\left(\partial_i A_0 - \partial_0 A_i\right) - \frac{1}{2}\beta\alpha^j h_{ij}\left(\partial_i A_0 - \partial_0 A_i\right)\right] + eA_0\mathbb{1}_4 + \left(1-\frac{1}{2}h_{00}\right)\beta mc^2
\end{aligned} \tag{137}$$

S10

$$S_{10} = \frac{-i\hbar^2}{16m^2c^2}\alpha^i\left(-2\partial_i\partial_j h_{0j} + \partial_j\partial_j h_{0i}\right) \tag{138}$$

$$iL_{S10}\left[\beta mc^2\right] = \frac{-\hbar^2}{8m}\beta\alpha^i\left(-2\partial_i\partial_j h_{0j} + \partial_j\partial_j h_{0i}\right) \tag{139}$$

After applying the unitary transformation S_{10}, the resulting transformed Hamiltonian, denoted as H^X is expressed as follows:

$$\begin{aligned}
\mathcal{H}^{X} &= -h_{0i}\Pi_i\mathbb{1}_4 + \frac{1}{2mc^2}\beta\alpha^i\alpha^j\left(1-\frac{1}{2}h_{00}\right)\Pi_i\Pi_j + \frac{i\hbar c}{4}\left[3\partial_i h_{0i}\mathbb{1}_4 - \partial_0 h_{ii}\mathbb{1}_4 - \alpha^i\alpha^j\partial_j h_{0i}\right] \\
&+ \frac{i\hbar}{4mc}\beta D_{ij}\Pi_i + \frac{\hbar^2}{8m}\beta\alpha^k\alpha^i\partial_k D_{ij} + \frac{i\hbar}{4mc}\left[\beta\alpha^i\alpha^j\partial_i h_{00} + \beta\alpha^i\alpha^k\partial_i h_{jk} + \frac{1}{2}\beta\alpha^i\alpha^j\partial_i h_{00}\Big|_{i\neq j}\right]\Pi_j \\
&+ \frac{1}{2mc^2}\left[-\frac{1}{2}\beta\alpha^i\alpha^k h_{jk}\left[\Pi_i, \Pi_j\right] - \beta h_{ij}\Pi_j\Pi_i\right] - \frac{i\hbar e}{2mc}\left[\beta\alpha^i\left(\partial_i A_0 - \partial_0 A_i\right) - \frac{1}{2}\beta\alpha^j h_{ij}\left(\partial_i A_0 - \partial_0 A_i\right)\right] \\
&- \frac{\hbar^2}{16m}\beta\partial_i\partial_i h_{00} + eA_0\mathbb{1}_4 + \left(1-\frac{1}{2}h_{00}\right)\beta mc^2
\end{aligned} \tag{140}$$

S11

$$S_{11} = -\frac{\hbar e}{4m^2c^3}\left(\alpha^i E_i - \frac{1}{2}h_{ij}\alpha^j E_i\right) \tag{141}$$

$$iL_{S11}\left[\beta mc^2\right] = \frac{i\hbar e}{2mc}\beta\alpha^i E_i - \frac{i\hbar e}{4mc}\beta\alpha^j h_{ij}E_i \tag{142}$$

$$iL_{S11}\left[-\frac{1}{2}h_{00}\beta mc^2\right] = -\frac{ihe}{4mc}\beta\alpha^i h_{00}E_i \tag{143}$$

After applying the unitary transformation S_{11}, the resulting transformed Hamiltonian, denoted as H^{XI} is expressed as follows:

$$\begin{aligned}\mathcal{H}^{XI} &= -h_{0i}\Pi_i\mathbb{I}_4 + \frac{1}{2mc^2}\beta\alpha^i\alpha^j\left(1-\frac{1}{2}h_{00}\right)\Pi_i\Pi_j + \frac{i\hbar c}{4}\left[3\partial_i h_{0i}\mathbb{I}_4 - \partial_0 h_{ii}\mathbb{I}_4 - \alpha^i\alpha^j\partial_j h_{0i}\right]\\ &+ \frac{i\hbar}{4mc}\beta D_{ij}\Pi_i + \frac{\hbar^2}{8m}\beta\alpha^k\alpha^i\partial_k D_{ij} + \frac{i\hbar}{4mc}\left[\beta\alpha^i\alpha^j\partial_i h_{00} + \beta\alpha^i\alpha^k\partial_i h_{jk} + \frac{1}{2}\beta\alpha^i\alpha^j\partial_i h_{00}\Big|_{i\neq j}\right]\Pi_j\\ &+ \frac{1}{2mc^2}\left[-\frac{1}{2}\beta\alpha^i\alpha^k h_{jk}\left[\Pi_i,\Pi_j\right] - \beta h_{ij}\Pi_j\Pi_i\right] - \frac{i\hbar e}{4mc}\beta\alpha^i h_{00}E_i - \frac{\hbar^2}{16m}\beta\partial_i\partial_i h_{00}\\ &+ eA_0\mathbb{I}_4 + \left(1-\frac{1}{2}h_{00}\right)\beta mc^2\end{aligned} \tag{144}$$

S12

$$S_{12} = \frac{-\hbar e}{8m^2c^3}\alpha^i h_{00}E_i \tag{145}$$

$$iL_{S12}\left[\beta mc^2\right] = \frac{i\hbar e}{4mc}\beta\alpha^i h_{00}E_i \tag{146}$$

After applying the unitary transformation S_{12}, the resulting transformed Hamiltonian, denoted as $H^{\mathcal{E}}$ is expressed as follows:

$$\begin{aligned}\mathcal{H}^{\mathcal{E}} &= -h_{0i}\Pi_i\mathbb{I}_4 + \frac{1}{2mc^2}\beta\alpha^i\alpha^j\left(1-\frac{1}{2}h_{00}\right)\Pi_i\Pi_j + \frac{i\hbar c}{4}\left[3\partial_i h_{0i}\mathbb{I}_4 - \partial_0 h_{ii}\mathbb{I}_4 - \alpha^i\alpha^j\partial_j h_{0i}\right]\\ &+ \frac{i\hbar}{4mc}\beta D_{ij}\Pi_i + \frac{\hbar^2}{8m}\beta\alpha^k\alpha^i\partial_k D_{ij} + \frac{i\hbar}{4mc}\left[\beta\alpha^i\alpha^j\partial_i h_{00} + \beta\alpha^i\alpha^k\partial_i h_{jk} + \frac{1}{2}\beta\alpha^i\alpha^j\partial_i h_{00}\Big|_{i\neq j}\right]\Pi_j\\ &+ \frac{1}{2mc^2}\left[-\frac{1}{2}\beta\alpha^i\alpha^k h_{jk}\left[\Pi_i,\Pi_j\right] - \beta h_{ij}\Pi_j\Pi_i\right] - \frac{\hbar^2}{16m}\beta\partial_i\partial_i h_{00} + eA_0\mathbb{I}_4 + \left(1-\frac{1}{2}h_{00}\right)\beta mc^2\end{aligned} \tag{147}$$

This matrix is already even to the desired order, thus concluding our transformations here.